

1 **Geomorphic imprint of high mountain floods: Insight from the 2022**
2 **hydrological extreme across the Upper Indus terrain in NW Himalayas**

3 Abhishek kashyap¹, Kristen L. Cook², Mukunda Dev Behera^{1*}

4 ¹Centre for Ocean, River, Atmosphere and Land Sciences (CORAL), Indian Institute of
5 Technology Kharagpur, Kharagpur- 721302, West Bengal, India

6 ²IRD, ISTerre, Université Grenoble Alpes, 1381 Rue de la Piscine, 38610 Gières, France

7 **Emails:**

8 Abhishek Kashyap: kashyap95abhishek@kgpian.iitkgp.ac.in

9 Kristen L. Cook: kristen.cook@univ-grenoble-alpes.fr

10 (*Correspondence): Mukunda Dev Behera: mdbehera@coral.iitkgp.ac.in

11

12

13

14

15

16

17

18

19

20 **Geomorphic imprint of high mountain floods: Insight from the 2022**
21 **hydrological extreme across the Upper Indus terrain in NW Himalayas**

22 **Abstract**

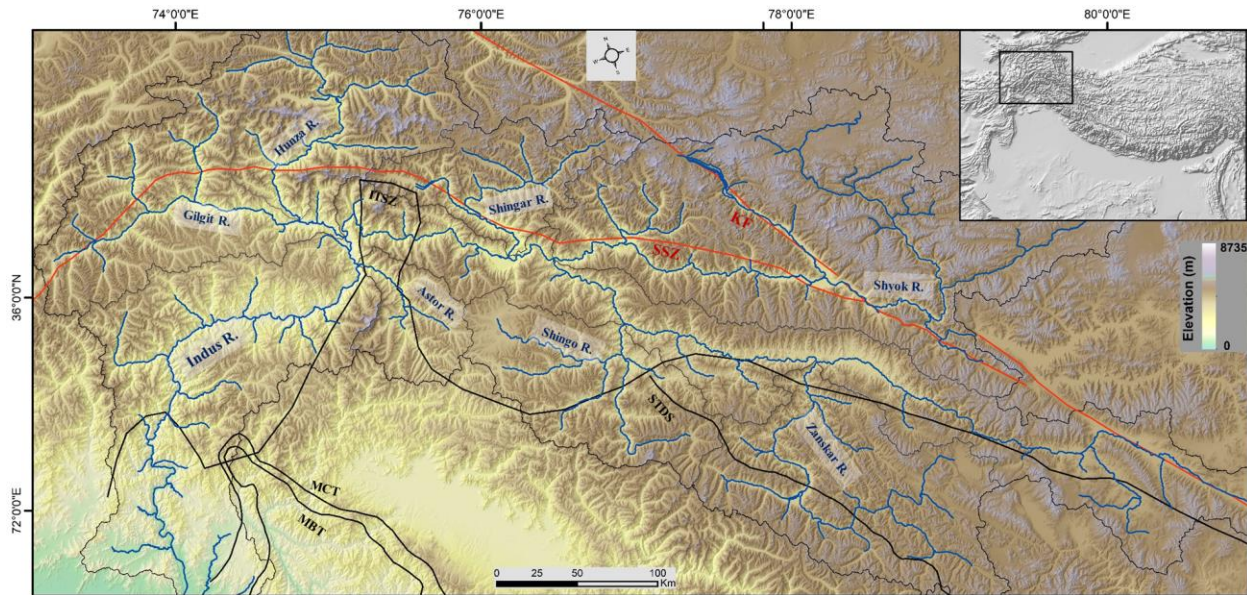
23 The interaction of tectonics, surface processes, and climate extremes impacts how the landscape
24 responds to extreme hydrological events. An anomalous precipitation event in 2022 occurred
25 during the monsoon season along the lower middle reaches of the Upper Indus River, resulting in
26 short-lived high-magnitude flooding and socioeconomic disruption downstream. To understand
27 the spatial relationship between the geomorphic response and climatic controls of this flood event,
28 as well as their primary triggers, we performed a landscape analysis using topographic metrics and
29 quantified the causal association between hydro-climatic variables. Temperature anomalies in
30 upstream glaciated sub-catchments had a considerable impact on snow cover distribution, based
31 on our observations. As snow cover changed, glacial melt runoff rose, contributing to increased
32 fluvial stream power after traversing higher-order reaches. The higher-order reaches of the Upper
33 Indus River received an anomalously high amount of precipitation, which, when combined with
34 substantial glacial melt discharge, contributed to an extreme flood across the high-relief steep
35 gradient channels. The flood-affected regions had a high mean basin k_{sn} and SL-index, including
36 numerous spikes in their magnitudes along their channel profiles downstream. To determine how
37 the lower middle reaches of the Upper Indus River responded to this flood event, we employed the
38 Enhanced Vegetation Index (EVI) and Normalized Difference Water Index (NDWI) as change
39 indicator metrics. We observed an inverse causal influence of NDWI on EVI and a statistically
40 significant relationship between anomalous stream power and relative EVI, suggesting that
41 downstream channel morphology changed rapidly during this episodic event and highlighting EVI
42 as a useful indicator of geomorphic change. We suggest that this extreme flood event is a result of
43 the interaction of anomalous glacial melt and anomalous precipitation over a high-relief landscape,
44 with a certain causal connection with anomalous temperature over the event duration. The synoptic
45 observations suggest that this meteorological condition involves the interaction of the Indian
46 Summer Monsoon (ISM) and Western Disturbance (WD) moisture fluxes. However, the
47 geomorphic consequences of such anomalous monsoon periods, as well as their influence on long-
48 term landscape change, are still unclear.

49 **Keywords:** anomalous precipitation; extreme flood; causal relationship; Upper Indus terrain

50 **1. Introduction**

51 High mountain floods in the Himalayas are associated with several processes, including coupling
52 of the Indian Summer Monsoon (ISM) and western disturbance (WD) circulations (Houze et al.,
53 2011), cloudbursts (Dimri et al., 2016), anomalous precipitation, cloud-scale interconnected
54 atmospheric anomalies (Dimri et al., 2017), and geomorphic driven surface processes (Sharma et
55 al., 2017). There is growing recognition that landscapes may evolve through the cumulative effects
56 of extreme episodic events, in particular in rapidly eroding terrains (Korup, 2012; Cook et al.,
57 2018). Recent studies suggest that even minor shifts in weather patterns can have a significant
58 impact on the frequency and magnitude of floods (Knox, 2000; Liu et al., 2015; Benito et al., 2015;
59 Sharma et al., 2022). It has also been suggested that high-magnitude flood occurrences in the
60 bedrock rivers draining the Himalayas are the geomorphic agents with the most significant impact
61 on the evolution of the regional landscape as well as on the residents of the downstream regions
62 (Bookhagen et al., 2005a; Sharma et al., 2017; Panda et al., 2020).

63 The Tibetan Plateau and its surrounding mountainous regions, such as the Himalayas and
64 the Karakoram ranges, are critical for the downstream hydrology and water availability of the
65 Indus River system (Hewitt, 2009; Immerzeel et al. 2010) (Fig.1). The majority of the hydrological
66 budget of Indus River comes from precipitation, snowmelt, and glaciers, but their relative
67 contribution varies among the major contributing tributaries (Bookhagen and Burbank 2010; Wu
68 et al., 2021). The Upper Indus catchment receives precipitation from two distinct climatic systems,
69 the WD and the ISM, over its foreland and highlands in the northwest (NW) Himalayas
70 (Bookhagen and Burbank 2006; 2010). However, it remains unclear yet how these two distinct
71 circulation patterns interact over the Himalayan landscape and what is their potential influence on
72 long-term geomorphic change (Dimri et al., 2015;2017; Ray et al., 2019).



73

74 Fig.1. Regional topographic setting of Upper Indus catchment along with its major tributaries
 75 overlaid with major geological structures (MBT= Main boundary Thrust, MCT= Main Central
 76 Thrust, STDS= Southern Tibet Detachment system, ITSZ= Indus Tibetan Suture Zone, SSZ=
 77 Shyok Suture Zone, KF= Karakoram fault).

78 Short-duration episodic weather events have a significant influence on hillslope-surface
 79 processes and rates of bedrock erosion by modulating mass movement and subsequent landscape
 80 evolution (Snyder et al., 2003; Bookhagen et al., 2005b; Srivastava et al., 2017). During such
 81 events, a lot of sediment is transported through the fluvial system, some of which is temporarily
 82 deposited in low-gradient reaches and changes the landscape, before being finally deposited in
 83 oceanic sinks (Goodbred, 2003; Panda et al., 2020). The geomorphic signatures of catchment
 84 morphology are vital for understanding and identifying the channel response involved in such
 85 events as well as the processes and patterns of erosion (Kashyap and Behera., 2023; Sharma et al.,
 86 2017).

87 From the beginning of July until the end of August 2022, large portions of the Indus catchment
 88 experienced unprecedented monsoon precipitation (Otto et al., 2023; Nanditha et al., 2023). Some
 89 recent studies suggest that the primary trigger of this anomalous precipitation event was an
 90 intensely low atmospheric circulation pattern, low sea surface temperatures across the eastern
 91 Pacific, and the advent of a La-Nina event (Otto et al., 2023; Nanditha et al., 2023). This extreme

92 precipitation event resulted in a catastrophic flood in the low elevation flood plains of the Indus
93 catchment (Jones, 2022; Otto et al., 2023; Ma et al., 2023). This severe flood had an extreme
94 impact over the southern province of Pakistan, causing internal displacement of about ~30–32
95 million people and the deaths of ~1500–1600 people (Bhutto, 2022; Khokhar, 2022; UNICEF,
96 2022; Ma et al., 2023). In excess of ~\$25–30 billion in economic losses are anticipated (Bhutto,
97 2022; Otto et al., 2023). According to reports, the flood in 2022 exceeded the peak flow rate of the
98 disastrous 2010 floods that occurred over Pakistan (Bhutto, 2022; UNICEF, 2022; Nanditha et al.,
99 2023). The magnitude of the fluvial discharge over the upstream tributaries of the Indus River
100 increased predominantly as a result of increased streamflow across glaciated channels (NDMA,
101 2022; UNICEF, 2022). However, the geomorphic consequences and the main drivers of this high-
102 magnitude flooding in the Upper Indus catchment have not been evaluated yet.

103 In the present study, we evaluated the spatial distribution of channel changes in the mountainous
104 portion of the Upper Indus catchment due to the extreme precipitation event in the months of July
105 and August 2022. We employed a channel slope-discharge product along the trunk channel of the
106 Upper Indus River to estimate the anomalies in the stream power resulting from the anomalous
107 precipitation event during July and August 2022. We used a random-forest-based machine learning
108 approach to compare the observed and predicted intensity of precipitation and runoff by assessing
109 the mean climatology of independent hydro-climatic variables. We further quantified the causal
110 relationship between hydro-climatic drivers using nonlinear time series data over the event
111 duration. We investigated the channel response of this episodic flood event by using the NDWI
112 and EVI as change indicator metrics and comparing that to event characteristics such as anomalous
113 precipitation, stream power, and channel metrics. We want to better understand the controls on
114 where and when these types of extreme hydrological events will substantially modify rivers and
115 landscapes so associated geomorphic hazards can be better anticipated, and we also want to better
116 constrain the potential role of these episodic events in driving long-term geomorphic change across
117 the western syntaxial region.

118 **2. Regional Setting**

119 In the Himalayas, the erosion rates are high and the landscape of the mountainous terrain is shaped
120 by the interactions between river systems and the basement tectonics (Jaiswara et al., 2019; 2020).

121 Among the Himalayan River systems, the Upper Indus is unique, including a fully developed,
122 ~1200-1400 km long, 8th- 9th-order drainage that enters the Himalayan terrain as an antecedent
123 channel and cuts right over the seismically active belt in the Indus- gorges (Fig. 1). This catchment
124 is highly affected by recurrent landslides or debris flows, and episodic glacial and landslide dams
125 that represent significant geomorphic hazards (Korup & Montgomery 2008; Korup et al., 2010).

126 The Upper Indus River flows through the highly tectonically active region of the Nanga
127 Parbat-Haramosh Massif (NP-HM), which is one of the highest relief regions on earth (~>5000
128 m), and has the strong potential to rapidly erode uplifted material (Leland et al. 1998; Shehzad et
129 al. 2009; Korup et al. 2010). The NP-HM region experiences the highest recorded rates of
130 denudation and channel incision on earth (~12 mm/y), as well as high rates of tectonic uplift (~4 -
131 10 mm/y) and forms river anticlines across extremely weak crust (Koons et al., 2002; 2013; Zeitler
132 et al., 2001; 2014; Butler, 2019). This has a significant impact on the tectonics and morphology of
133 the western Himalayas (Hewitt, 2009; Zeitler et al., 2014). The Upper Indus catchment (UIC) is
134 characterized by extremely steep channel gradient of ~>20-25°, high topographic relief of ~4000–
135 5000 m, and a large portion of snow-covered peaks (Hewitt, 2007; Farinotti et al., 2020).

136 As a fraction of the total annual discharge, snowmelt constitutes up to 50% in the Upper-
137 Indus catchment (UIC) (Burbank & Bookhagen, 2006; 2010; Scherler et al., 2011). Due to the
138 Western Disturbance (WD) inclination, the UIC has a lot of precipitation in the winter and spring
139 (Kapnick et al., 2014), while due to the orographic barrier of the high mountains, the influence of
140 the ISM in the region weakens towards to the north-west (Forsythe et al., 2017). The annual
141 precipitation in the UIC increases with the elevation; across the northern valley floors- in the rain
142 shadows it ranges from 100-200 mm/y; while at elevation ~4000-4400 ma.s.l., it ranges from 600-
143 800 mm/y; and above >~5000 ma.s.l., it ranges from 1500 -2000 mm/y (Sharif et al., 2013; Wu et
144 al., 2021). From October to March, the monthly mean temperatures in the UIC are below freezing
145 at elevations > ~3000 m (Archer, 2004). Discharge in the tributary channels of the Upper Indus
146 River that depend on glacier meltwater has a strong association with summer time mean air
147 temperatures across the Karakoram ranges (Forsythe et al., 2017; Wu et al., 2021).

148 **3. Materials and Methodology**

149 **3.1 Data Used**

150 In the present study, we used a 30 m SRTM digital elevation model (DEM) for landscape
151 characterization and geomorphic quantitative parameter estimation. To investigate the impact of the
152 climatic variables driving this extreme event on regional erosion processes, we utilized daily
153 precipitation datasets spanning 40 years (1982–2022) from July 1 to August 31 from CHIRPS
154 (Climate Hazards Group Infrared Precipitation with Station Data) (Version 2.0 Final). Several
155 previous studies have investigated CHIRPS precipitation datasets at daily, monthly, and annual
156 temporal scales across the Indus Basin (Gao et al., 2018; Ullah et al., 2019; Nawaz et al., 2021;
157 Shahid et al., 2021). In their studies, they extensively evaluated CHIRPS's performance against
158 regional ground datasets obtained from meteorological stations. Several studies (Katsanos et al.,
159 2016, Paredes-Trejo et al., 2017, Bai et al., 2018, Gao et al., 2018) suggest CHIRPS for
160 hydrological analysis and water resource management due to its fine spatiotemporal resolution.

161 We investigated the spatiotemporal distribution of hydrometeorological variables using daily
162 datasets from July 1 to August 31. The ERA5-Land Daily Aggregated-ECMWF Climate
163 Reanalysis, which had a spatial resolution of 11132 meters, provided data on 2-meter air
164 temperature, skin temperature, dewpoint temperature, snowmelt, and runoff. We used remote
165 sensing-based indices to detect signatures of anomalous changes over the landscape. We computed
166 these metrics over the monthly mean for July and August 2022, using daily datasets of the MODIS-
167 based normalized difference water index (NDWI), the normalized difference snow index (NDSI),
168 snow albedo, EVI, and surface reflectance bands b1 and b2, which have a 500-meter spatial
169 resolution.

170 **3.2 Drainage network extraction and landscape analysis.**

171 We extracted the drainage network from the DEM using the ArcGIS platform. A regional slope
172 map was produced by running a 1000 m radius mean filter over the slope model derived from the
173 DEM, and a regional relief map was generated by passing a 1000 m circular radius focal range
174 window over the DEM. Further analysis of the DEM and the derived flow accumulation data were
175 performed in MATLAB using the transient profiler tools (Jaiswara et al., 2019, 2020). We
176 extracted the longitudinal profiles of the bedrock channels within an accumulation region of about
177 $1 \times 10^6 \text{ m}^2$ and channel network of the Upper Indus catchment using TopoToolbox (Wobus et al.,
178 2006; Kirby and Whipple, 2012; Schwanghart and Scherler, 2014). We used a 1000 m smoothing

179 window and a 20 m vertical interval to sample the channel networks in order to reduce the noise
180 and artefacts that are embedded in the elevation data.

181 **3.3 Quantitative Geomorphic parameters**

182 We used geomorphic quantitative parameters such as SL (Stream length-gradient index)-index, k_{sn}
183 (Normalized steepness index) and Stream power of the Upper Indus trunk channel to evaluate the
184 influence of the high magnitude flooding event across the Upper Indus River during July and
185 August 2022. To evaluate the spatial variability of the flood magnitude and the channel
186 morphology, these metrics are plotted on the longitudinal profile of the trunk channel.

187 **3.3.1 Stream length-gradient index (SL- Index)**

188 Rivers often achieve an equilibrium or steady state between erosion and sedimentation, which is
189 represented by a concave longitudinal river profile (Schumm et al., 2002). Tectonic, lithological,
190 and/or climatic factors often result in shifts in river profiles from this expected steady-state
191 condition (Hack, 1973; Burbank and Anderson, 2011). Here, we use the Stream Length-Gradient
192 (SL) index to identify the zones of topographic break and changes in the channel gradient of the
193 longitudinal profile by using the equation:

$$194 \quad SL = (\Delta H/\Delta L)/L \dots \dots \dots (1)$$

195 where SL denotes the steepness or gradient of the profile for the local reach, L is the total river
196 length from the midpoint of the local reach to the highest point on the channel, ΔH is the change
197 in elevation over the reach and ΔL is the length of the reach, so $\Delta H/\Delta L$ represent the channel slope
198 or gradient of the reach. A sharp lithological variation and/or the differential uplift across active
199 structures are frequently linked to an abrupt change in SL-index along the river (Hack, 1973;
200 Jaiswara et al., 2020; Kashyap et al., 2024).

201 **3.3.2 Channel Steepness index**

202 We extracted the bedrock profile of the Upper Indus River, which can be described using the power
203 law relationship between upstream drainage area (A) and channel gradient (S) as (Jaiswara et al.,
204 2019, 2020; Kashyap et al., 2024):

205
$$S = k_s A^{-\theta} \dots \dots \dots (2)$$

206 where $k_s = (E/K)1/n$ is the channel steepness index, $\theta = (m/n)$ is the channel concavity index, m
 207 and n are positive constants, E is the erosion rate at a steady state (Wobus et al., 2006; Kirby and
 208 Whipple, 2012). The relative magnitude of k_s is often related to the surface uplift rate as well as
 209 the erosional efficiency across a bedrock catchment (Snyder et al., 2003; Wobus et al., 2006).

210 **3.3.3 Stream Power estimation**

211 The normalized steepness index (k_{sn}) has emerged as an important topographic metric with
 212 significant correlation with erosion rate over a wide range of timescales (Wobus et al., 2006;
 213 Jaiswara et al., 2019; Kashyap et al., 2024). However, one major drawback of k_{sn} is that it includes
 214 an assumption of spatially constant precipitation because upstream drainage area is used as a proxy
 215 for discharge (Adams et al., 2020; Leonard et al., 2023a).

216 In the present study, we incorporate the precipitation intensity into the stream power
 217 calculation to analyze the anomalous stream power along the trunk channel during the flood event.
 218 We estimate the precipitation induced stream power using the slope-discharge method, which
 219 involves multiplying the accumulated flow distance weighted by precipitation with the hyperbolic
 220 tangent function of the channel gradient along the flow path (Adams et al., 2020; Leonard et al.,
 221 2023b). The estimation of stream power ($K_{sn}Q$) as a function of channel discharge can be estimated
 222 as:

223
$$K_{sn}Q = (S) \times f(\int p * FD) \dots \dots \dots (3)$$

224 where S is the channel gradient, FD is the accumulated flow distance, p is the accumulated
 225 precipitation (Leonard et al., 2023a; b). Thus, $K_{sn}Q$ is a normalized version of the channel
 226 steepness metric that uses the product of channel gradient (S) and upstream discharge (Q)
 227 estimated from mean precipitation (P) as a fluvial discharge proxy. This enables $K_{sn}Q$ to account
 228 for the spatial and temporal variability in precipitation along the upper Indus River during the high
 229 magnitude flood event. Accumulated precipitation resolves spatial patterns well and scales nearly
 230 linearly with relevant discharges, particularly for large and long-lasting precipitation events (Rossi
 231 et al., 2016; Leonard et al., 2023a; b).

232 **3.4 Machine learning based approach to model the anomalous event characteristics**

233 The Random Forest (RF) technique is a supervised machine learning method that has been used
234 as a tree-based ensemble technique and includes a bagging or boot-strapping algorithm (Breiman,
235 2001; Wolfensberger et al., 2021). In the present study we use a RF based multivariate regression
236 approach to estimate the anomalous precipitation and runoff intensity in July and August 2022
237 using the independent variables obtained from classifying variable importance.

238
$$H(x) = \sum_{i=1}^T hi(x)..... (4)$$

239 Where, $hi(x)$ denotes the i^{th} regression tree output (hi) on sample x . Therefore, the prediction of
240 the RF is the mean of the predicted values of all the decision trees. T denotes the regression trees
241 for regression prediction.

242 Based on the mean climatology of the last 40 years, we predict the daily anomalous
243 precipitation and runoff intensity for the 2022 event and compare them with the observed actual
244 values. We employed the highest significance variables, as well as precipitation and runoff data
245 from 1982 to 2021, as a training set. We utilized a time series cross-validation approach in this
246 study to evaluate the Random Forest model's performance in predicting precipitation and runoff
247 during the Upper Indus catchment's high-elevation flood event in July and August 2022. Given the
248 temporal dependency and sequential pattern of hydro-climatic data, using a normal K-fold cross-
249 validation method could result in data leakage by allowing future data to inform past projections.
250 To address this issue, we employed time series cross-validation to maintain the data within
251 chronological order. We trained the model using a sliding window method, gradually moving the
252 training window forward in time with each iteration. Specifically, we designed the first training
253 window to contain data from the first 30 years, leaving the last 10 years for testing. In each
254 successive iteration, we increased the training window by one year and retrained the model on the
255 expanded training set. We trained these models on meteorological variables obtained from the
256 classification of the most significant, as well as other physical drivers associated with high-
257 elevation flood episodes in the region. We evaluated the model's performance based on the
258 accuracy of precipitation and runoff predictions, using metrics such as mean absolute error (MAE),
259 mean squared error (MSE), and root mean squared error (RMSE) (SI. Table. 1- 2). We computed
260 these metrics for each rolling window to gain insight into the model's performance across various

261 time periods, especially in the lead-up to the 2022 flood event. To utilize the independent variables
262 to estimate these event characteristics, we first classify the hydro-climatic variables based on their
263 higher importance using the RF classification approach. Then, by using the RF multivariate
264 regression approach, we select only those independent variables with the highest significance to
265 estimate anomalous precipitation and runoff intensity during the event duration.

266 **3.5 Causal discovery among Hydro-climatic variables**

267 Causal methodologies have been utilized to evaluate whether and how changes in one hydro-
268 climatological variable during anomalous extreme events influence the magnitude of another
269 (Runge et al., 2019a; Nowak et al., 2020). To understand how an extreme event is regulated over
270 high mountainous terrain, a temporal investigation of event characteristics is required. Using this
271 evaluation, we gain insight into how the conditioning hydro-climatic variables that regulate these
272 extreme events evolve throughout event duration in a catchment (Runge, 2018; Krich et al., 2020).
273 Understanding directional dependencies is crucial to distinguish them from connections that
274 cannot be deduced using any statistical model (Kretschmer et al., 2017; Karmouche et al., 2023).

275 In this study, we use causal stationarity, and the absence of contemporaneous causal effects
276 for the time series datasets using the PCMCI and MCI approaches (Tibau et al., 2022; Runge,
277 2023). PCMCI is a causal identification technique that combines the Momentary Conditional
278 Independence (MCI) approach with the PC algorithm (Runge et al., 2019b; Nowack et al., 2020).
279 Given a set of multivariate time series, PCMCI estimates the time series graph that depicts the
280 conditional independencies among the time-lagged factors (Runge et al., 2014; 2019a). In addition
281 to PCMCI, we use the ParCorr linear independence test based on partial correlations is employed
282 (Runge et al., 2014; 2023).

283 In order to evaluate the meteorological disturbances associated with the Upper Indus Flood of
284 2022, we identified the causal lag-connection between hydroclimatic variables, with a specific
285 focus on exploring the meteorological conditions leading up to and during the flood event. We
286 focused on identifying the short-term meteorological drivers that triggered the anomalous
287 precipitation-driven high elevation flood and understanding the distribution of its immediate
288 impacts within the Upper Indus catchment. We emphasize that this study does not attempt to
289 explore the causality of long-term climatic changes or assess the full geomorphic consequences of

290 the flood on the landscape. We deliberately limit the scope to comprehend the meteorological
291 conditions and their direct impact on the flood in the July-August 2022 period. By narrowing our
292 focus to the short-term hydro-climatic interactions, we aim to offer insights into the key
293 atmospheric processes and their role in shaping the event's severity rather than its broader or
294 longer-term geomorphic impacts.

295 In the present study we use the daily datasets of hydro-climatological variables and group them
296 as; Temperature gradient (Tg), including Air temperature, Surface temperature, and Dewpoint
297 temperature; Rainfall gradients (Rg), including Precipitation intensity, Runoff and Snowmelt; and
298 anomalous change indicators (Ac) including EVI, NDWI, and NDSI, July 1 to August 31, 2022,
299 so includes 62 observational intervals. We evaluate the causal interference between these hydro-
300 climatic variables using the MCI approach with a maximum 2-day lag period ($\tau_{\max} = 2$) and a limit
301 for significance set to 0.05 ($\alpha = 0.05$), in order to examine the spatially interdependence
302 relationships among each of these variables during 2-day event periods.

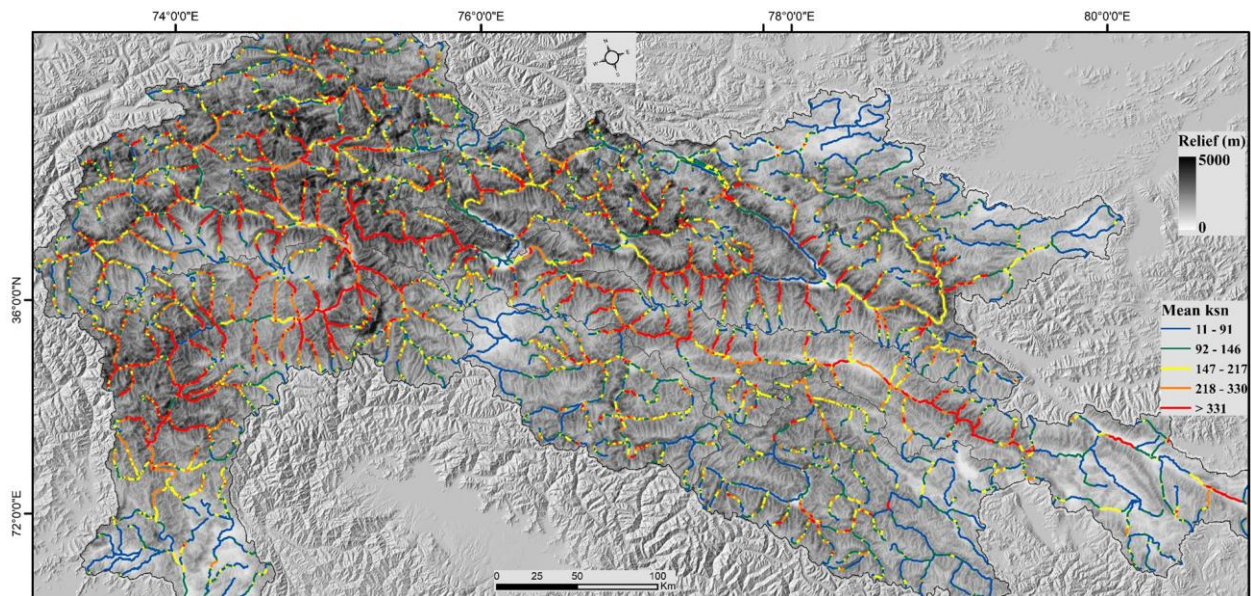
303 **3.6 Moisture pathways**

304 The Hybrid Single-Particle Lagrangian Integrated Trajectories (HYSPLIT) model
305 (https://www.ready.noaa.gov/HYSPLIT_traj.php) has been employed to determine the probable
306 moisture parcel source region (Joshi et al., 2023). Over the past decade, researchers have used the
307 HYSPLIT model to identify moisture sources (Wang et al., 2017; Joshi et al., 2023). To determine
308 the backward trajectory following an anomalous precipitation event, this study used the HYSPLIT
309 model. We used three starting heights of 500, 1000, and 3000 ma.s.l. to calculate the backward
310 trajectory for each day of July and August 2022, given that the HYSPLIT model required the start
311 date/time, location, and height for each precipitation event (Wang et al., 2017; Gudipati et al.,
312 2022). This study used meteorological data with a spatial resolution of $1^{\circ} \times 1^{\circ}$ from the Global Data
313 Assimilation System (NCEP-GDAS).

314 **4. Results**

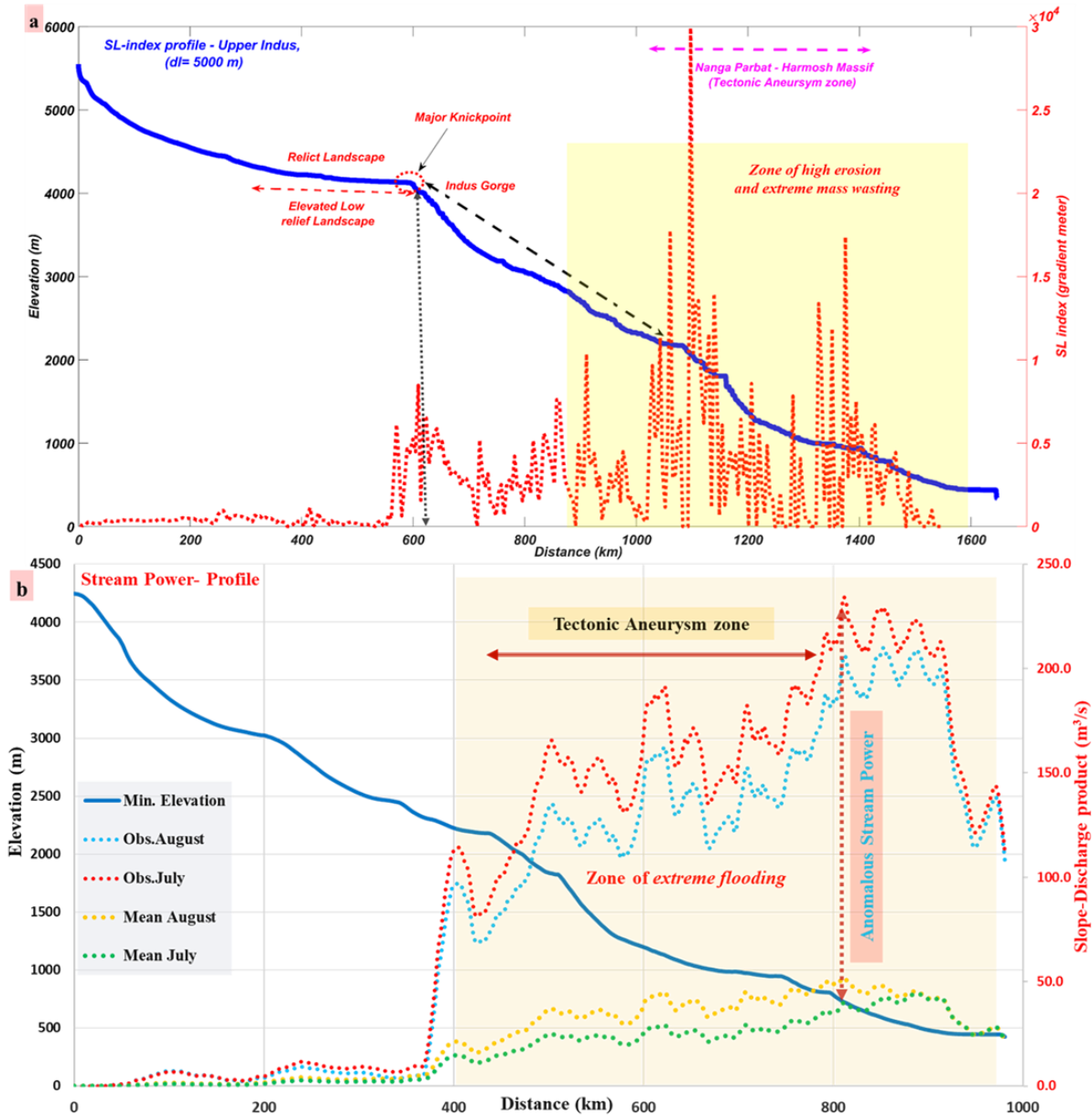
315 **4.1 Geomorphic analysis of the Upper Indus terrain**

316 The Indus River is around ~1400–1600 km long and forms multiple loops both parallel to and in
 317 opposition to the regional structural trend; its bed elevation ranges from ~500-6000–m. The river
 318 exhibits distinct morphological characteristics over its flow path in terms of its topographic
 319 attributes and derivatives. Over the elevated low-relief landscape in the Tibetan plateau, the relief
 320 and channel gradient vary as ($\sim 0-500$ m; $\sim 0-10^\circ$), with a low SL index ($\sim <1 * 10^4$) gradient meter
 321 and mean basin k_{sn} of ($\sim <90$ m^{0.9}) (Fig. 2; Fig. 3a). Then, when the river traverses through the NP-
 322 HM region, there is a progressive rise in the local relief and channel gradient to ($\sim >2000-3000$ m;
 323 $\sim >25-35^\circ$), which is also reflected in the SL-index ($>2.5-3 \times 10^4$) and mean k_{sn} ($\sim >331$ m^{0.9}). This
 324 region is characterized by topographic discontinuities across active structures, leading to high
 325 relief variation and topographic roughness.



326
 327 Fig.2. Spatial distribution of local relief overlaid with Mean basin k_{sn} ranges across the Upper
 328 Indus River catchment.

329 The tributaries in the upstream glaciated valleys that flow parallel to the structural trend
 330 have a higher mean channel gradient ($> \sim 20-30^\circ$) and topographic relief ($> \sim 2000-3000$ m) (Fig. 2).
 331 When these tributary channels start to descend towards the main stream after following the
 332 glaciated landscape, the value of SL and k_{sn} for the trunk channels shows a significant rise at
 333 $\sim 3000-4000$ m mean elevation. Approaching the southern mountain front, the main trunk channel
 334 relief and channel gradient are $\sim 1000-2000$ m and $\sim 15-25^\circ$ respectively (Fig. 3a).



335

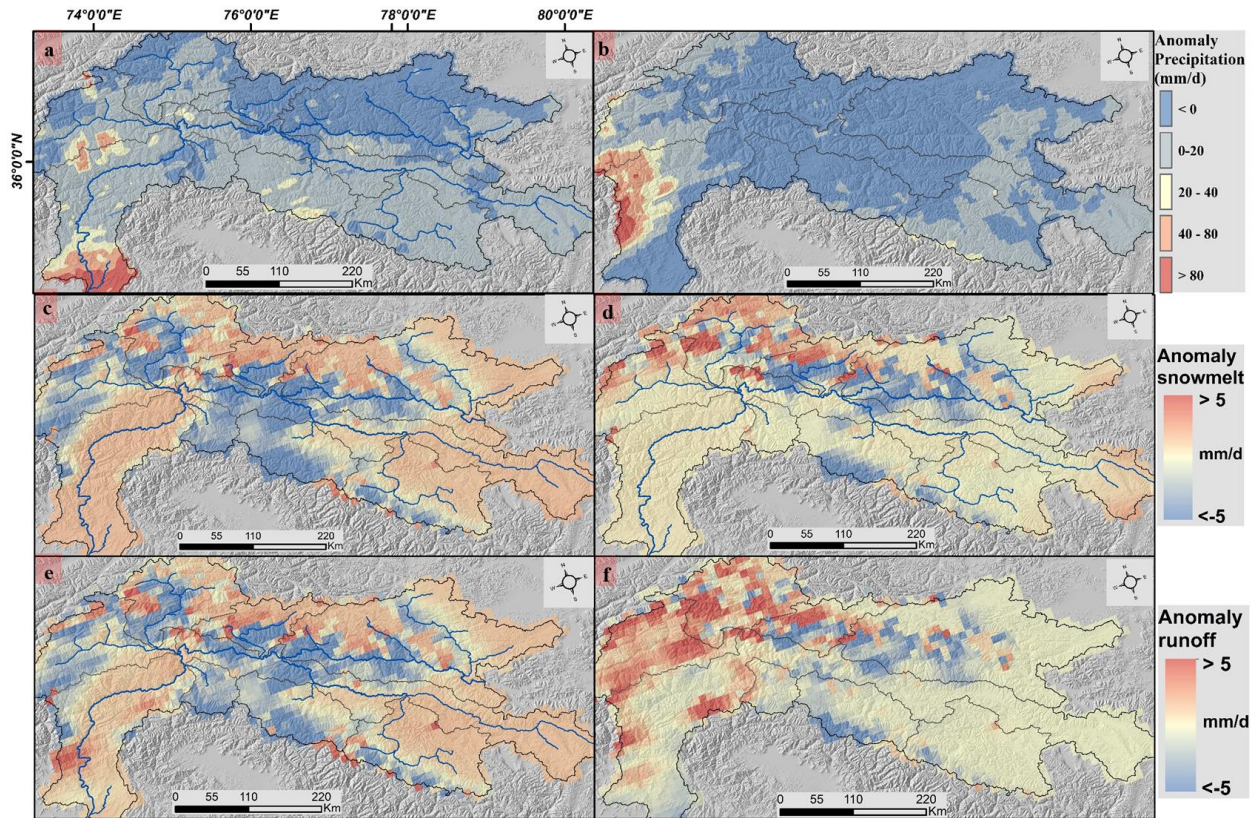
336 Fig.3. The trunk channel profile of Upper Indus River plotted with (a) SL-index; (b) The highest
 337 order profile of Upper Indus River plotted with Stream power (slope-discharge product)-channel
 338 elevation (highest order profile is the subset of trunk channel profile indicated by black dash line).

339 The spatial association of higher k_{sn} ($>\sim 331 m^{0.9}$), topographic relief ($\sim 1500-2000 m$), and
 340 longitudinal increase in channel gradient along the main Upper Indus River channel downstream
 341 suggests a higher erosional regime. These high values for the various topographic metrics highlight
 342 zones of accelerated erosion where the river is in gradational disequilibrium. Furthermore, this

343 tectonically active southern front coincides with a region that gets significant annual mean
344 precipitation (~1500–2500 mm/y), suggesting a tectonic-climate linkage in the erosional process.

345 **4.2 Spatial distribution of Hydro-climatic anomalies over event duration**

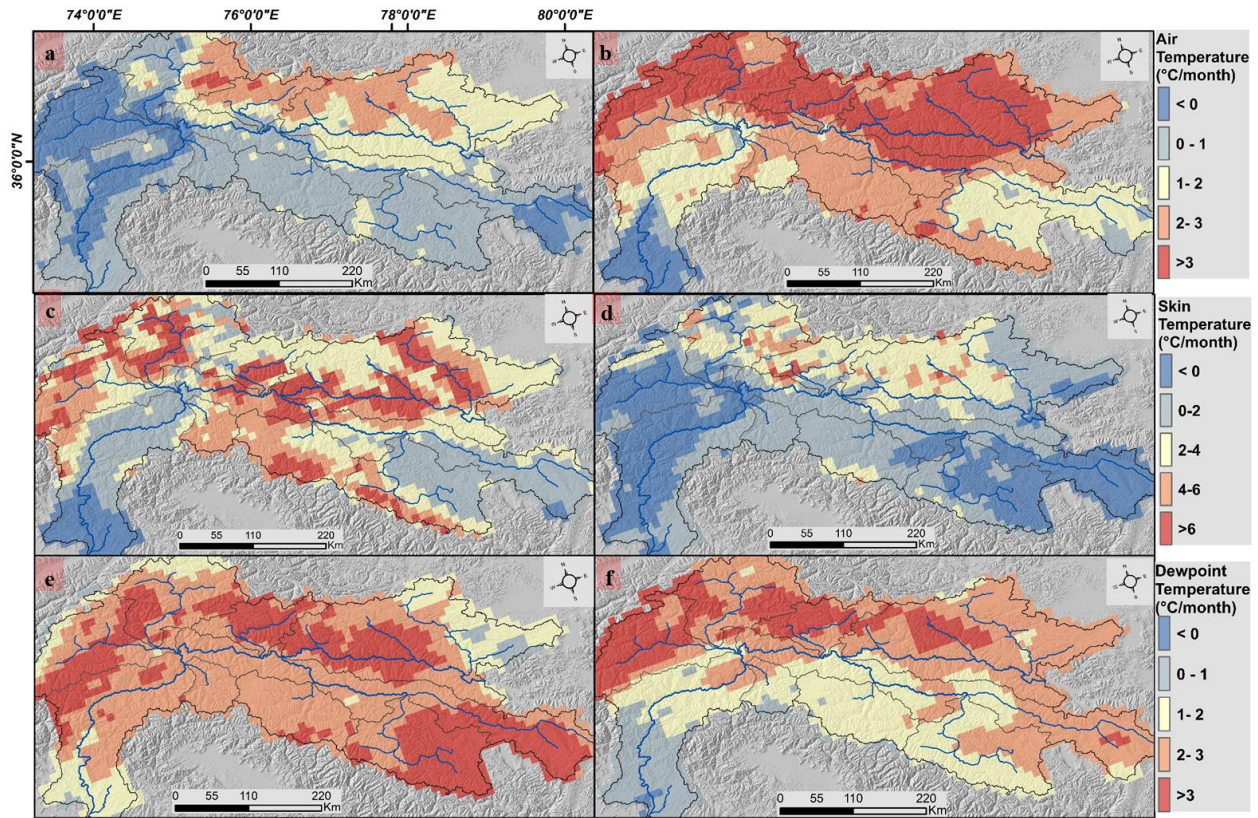
346 The downstream reach of the Upper Indus trunk channel received a significant amount of
347 anomalous precipitation (>~60–80 mm/d) during the observation period of July and August 2022
348 (Fig. 4a, 4b). The spatial variability of anomalous precipitation varies with a range of >~0–40
349 mm/d along its major glaciated tributaries, such as Hunza, Astor, Gilgit, Shingo, and Zaskar. In
350 July and August 2022, the total extent of anomalous precipitation was around ~900–1000
351 mm/month, which was approximately ~300–400% more than the long-term (1982–2022) mean
352 climatology. From July to August 2022, there was continuous precipitation in the high gradient
353 downstream region, and due to the antecedent weather conditions, extreme precipitation likely
354 produced suitable conditions for high-magnitude flooding. The potential geomorphic response of
355 such anomalous precipitation is suggested by the resulting anomalous stream power over the
356 downstream channels (Fig. 4c, 4d). The spatial distribution of anomalous stream power shows that
357 the greatest increase occurred at ~400-800 km along the channel profile downstream. For both the
358 months of July and August of 2022, we observed a significant rise in the stream power, to ~>200
359 m³/s above the mean values (Fig. 3b).



360

361 Fig. 4. Spatial distribution of hydro-meteorological variables for anomalous July and August
 362 month of 2022 across Upper Indus catchment such as: (a) precipitation (July) (b) precipitation
 363 (August) (c) Snowmelt (July) (d) snowmelt (August); (e) Runoff (July) (f) Runoff (August).

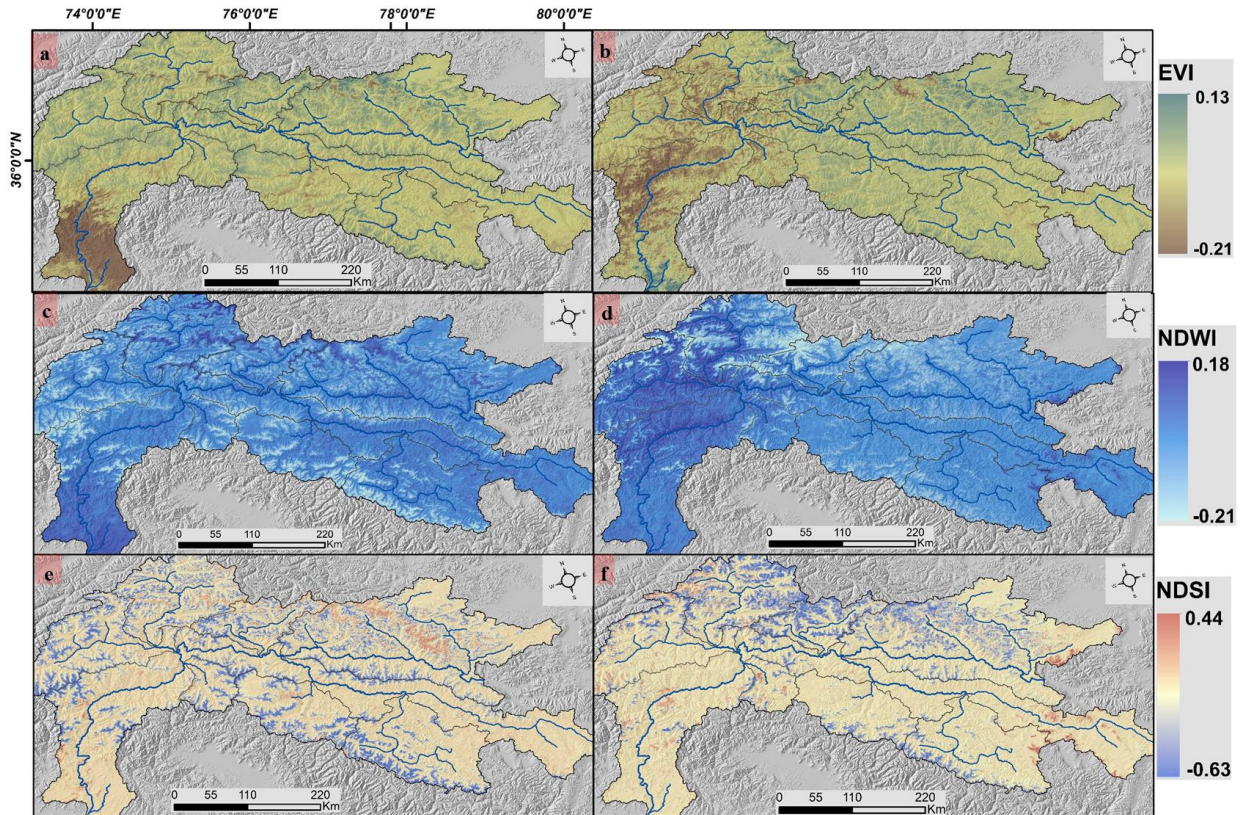
364 During the observation period, other variables, such as runoff and snowmelt, also showed
 365 positive anomalies across the upstream glaciated sub-catchments over the Karakoram ranges (Fig.
 366 4e, 4f). Furthermore, during July and August 2022, the temperature variables indicated a positive
 367 deviation from the mean climatological trend over the glaciated catchments. In the upstream sub-
 368 catchments in Shyok, Shingar, Hunza, and Gilgit, air and dewpoint temperatures reach ($> \sim 3^{\circ}\text{C}$
 369 above mean), while surface temperatures reach ($> \sim 6^{\circ}\text{C}$ above mean) (Fig. 5). The spatial
 370 distribution of anomalous temperatures corresponds well with the anomalous snowmelt and runoff
 371 magnitude across the upstream glaciated catchments.



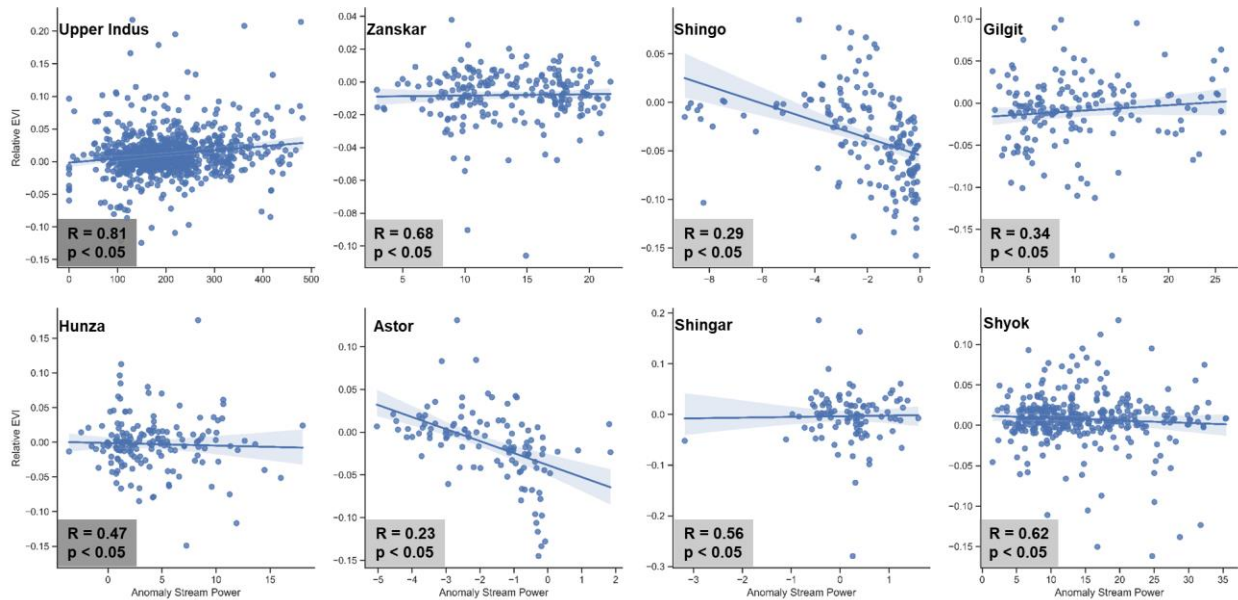
372
 373 Fig. 5. Spatial distribution of hydro-meteorological variables for anomalous July and August
 374 month of 2022 across Upper Indus catchment such as: (a) Air temperature (July) (b) Air
 375 temperature (August) (c) Surface temperature (July) (d) Surface temperature (August); (e)
 376 Dewpoint temperature (July) (f) Dewpoint temperature (August).

377
 378 We also observed a significant shift in the spatial distribution of change indicator variables
 379 during the observation period. In July 2022, the lower middle reaches of the Upper Indus River
 380 exhibited a negative change in EVI (~ -0.21) and a positive relative NDWI ($\sim 0.15-0.20$). This
 381 inverse relationship between these two change indicators was found in the upstream channel as
 382 well in August. During the event, the tributary channels in the upstream glaciated landscape
 383 experienced a significant change in snow cover distribution, as demonstrated by the spatial
 384 variations of the relative NDSI ($\sim 0-0.63$). Changes in relative snow cover correspond directly to
 385 increases in snowmelt and glacial runoff across glaciated catchments (Fig. 6). We observed a
 386 significant relationship ($p < 0.005$; $R = 0.81$) between the relative EVI metric and the anomalous
 387 stream power in the Upper Indus trunk channel and along its main tributaries. The anomalous
 388 stream power of the Upper Indus River and all of its major tributaries corresponds to a proportion

389 of EVI change that exceeds across low-gradient regions. This positive relationship with an
 390 increasing trend suggests a substantial geomorphic response due to extreme flooding. However, a
 391 negative relationship between anomalous stream power and EVI can also be observed across the
 392 channels of Astor and Shingo (Fig. 7).



393
 394 Fig. 6. Spatial distribution of hydro-meteorological variables for anomalous July and August
 395 month of 2022 across Upper Indus catchment such as: (a) EVI (July) (b) EVI (August) (c) NDWI
 396 (July) (d) NDWI (August); (e) NDSI (July) (f) NDSI (August).



398

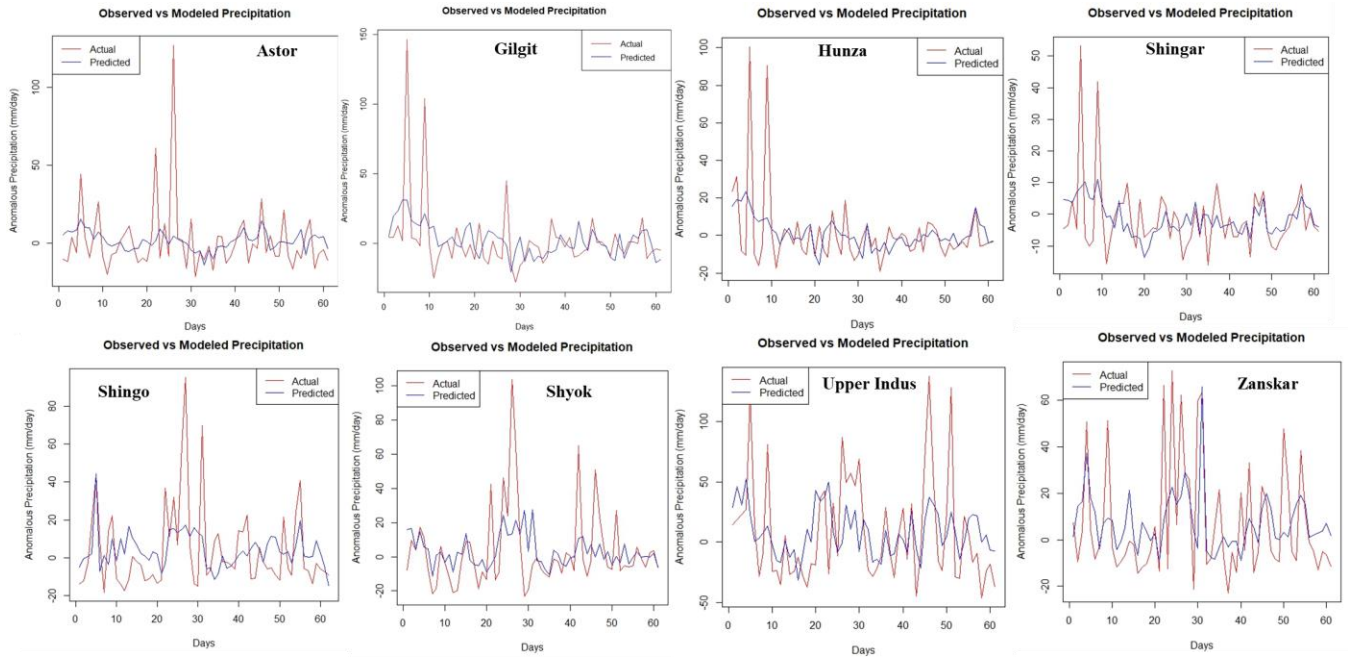
399 Fig.7. Statistical relationship between Relative EVI- Anomalous Stream Power from July 1 to
 400 August 31, 2022 across Upper Indus catchment as well as along its all the major tributaries.

401 4.3 Machine learning based approach to quantify the event anomalies

402 The RF-classification-based determination of variable importance indicates that dewpoint
 403 temperature is the most significant variable in estimating precipitation intensity. Other significant
 404 variables include surface temperature and air temperature. Relative NDSI was the variable of
 405 highest significance for estimating precipitation in all other sub-catchments except Shingar (Fig.
 406 S1). Snowmelt, dewpoint temperature, relative NDSI, and surface temperature are the most
 407 significant variables for each sub-catchment when estimating runoff intensity. Surface temperature
 408 holds higher significance in the trunk channel catchment of the Upper Indus, followed by air
 409 temperature and precipitation intensity (Fig. S2). The anomalous precipitation and runoff intensity
 410 are then estimated using these independent variables with the highest significance obtained during
 411 classification.

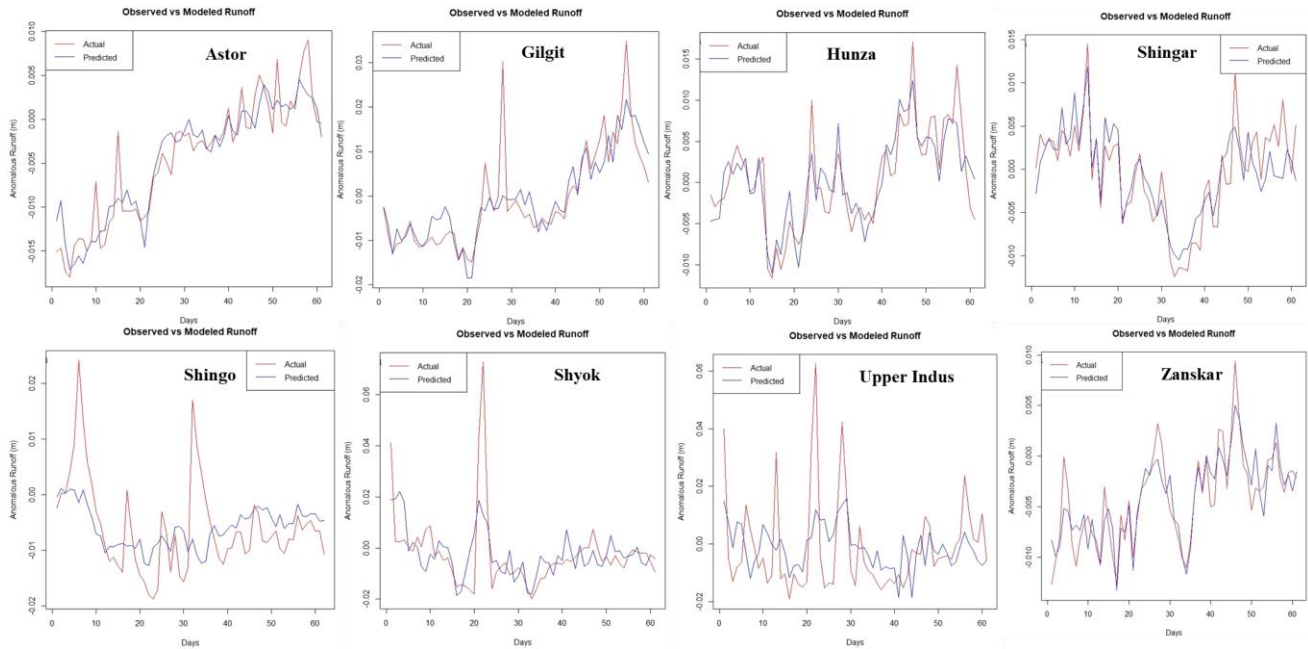
412 The results show that the Upper Indus catchment received significantly more precipitation
 413 and runoff than predicted at multiple instances in July and August of 2022 (Fig. 8). The anomalous
 414 and extreme characteristics of the hydro-climatic and terrestrial drivers could explain this
 415 phenomenon. The Upper Indus catchment received a significant amount of anomalous

416 precipitation, with an intensity of $>\sim 100$ mm/d, which is much higher than the predicted intensity
 417 during the period of observation. The channels in the higher relief landscapes such as Astor and
 418 Gilgit encountered the second-highest anomalous incidence, with intensities $\sim 80\text{--}100$ mm/d. The
 419 upstream glaciated catchments, such as the Shyok, Shingo, and Hunza, also have persistent
 420 anomalous intensities of up to ~ 100 mm/d. The least impacted catchment was Zanskar and Shingo,
 421 despite a high rate of precipitation that ranges from $\sim 60\text{--}80$ mm/d.



422
 423 Fig. 8. Random Forest-Regression based observed vs modeled anomalous precipitation from July
 424 1 to August 31, 2022 across Upper Indus catchment as well as along all the major tributaries.

425
 426 The distribution of observed and predicted runoff shows the intensity of observed runoff
 427 corresponds with the precipitation trend. During the observation period, the Upper Indus
 428 catchment had much higher runoff rates, followed by upstream glaciated sub-catchments including
 429 Shyok ($\sim 30\text{--}60$ mm/d), Shingo, and Gilgit ($\sim 20\text{--}30$ mm/d). However, in the majority of the
 430 upstream sub-catchments, the observed anomalous runoff intensity is insignificant (Fig. 9).



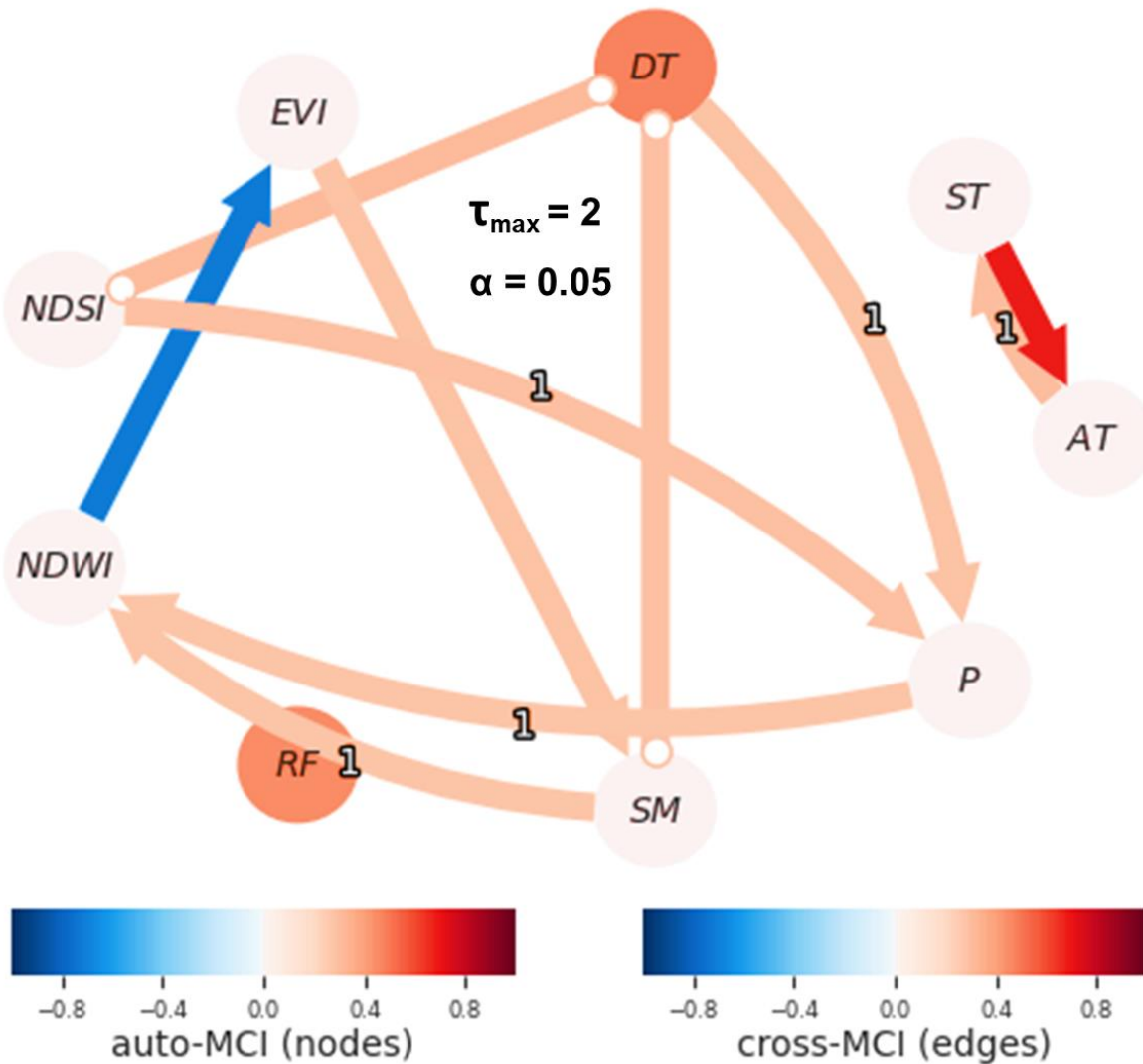
431

432 Fig. 9. Random Forest-Regression based observed vs modeled anomalous runoff from July 1 to
 433 August 31, 2022 across Upper Indus catchment as well as along all the major tributaries.

434 **4.4 Causal relationship among Hydro-climatic variables over event duration**

435 The causal analysis showed that the impact of numerous meteorological variables on the extreme
 436 flood over the Upper Indus terrain varied significantly. We observed a significant causal lagged
 437 connection between dewpoint temperature and NDSI, which together positively influenced
 438 precipitation intensity with a 1-day lag across the Upper Indus catchment. Similarly, precipitation
 439 intensity and snowmelt exhibit a positive causal influence on NDWI with a 1-day lag period. For
 440 instance, the cross-correlation between precipitation and dewpoint temperature with positive
 441 impact is > 0.4 over the event duration. There was a significant negative causal influence of NDWI
 442 on EVI, indicating an inversely proportional relationship across the observational lag period. The
 443 hydro-climatic variables such as precipitation intensity, snowmelt, NDWI, EVI, NDSI, air
 444 temperature, and surface temperature, had non-linear and non-stationary trends from July 1, 2022,
 445 to August 31, 2022, as shown by the autocorrelation and PCMCi magnitude over the time series.
 446 The auto MCI ranges of these variables are comparatively very low. Runoff and dewpoint
 447 temperatures exhibit stationarity and a linear trend over the time series with relative high auto-
 448 MCI ranges. It is also observed that dewpoint temperature has a significant inherent connection

449 with snowmelt and NDSI, indicating that these variables have a direct causative relationship with
 450 a high cross-MCI range (Fig. 10). In a causal investigation, edges with arrows indicate a link
 451 between the drivers. However, depending on the available metrics, there may be an instant causal
 452 connection between the drivers. It should be observed that this relationship may not have been
 453 determined to be causative.



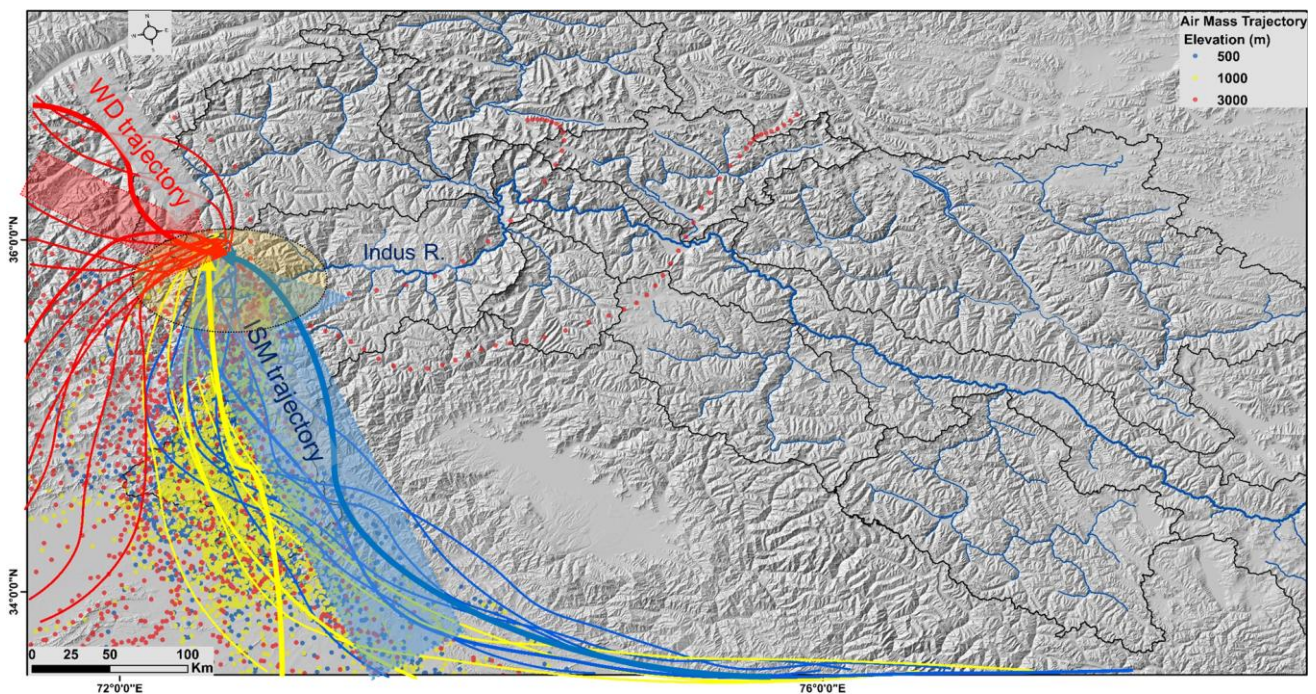
454

455 Fig.10. Causal detection among hydro-climatic driver having non-linear time series from July 1 to
 456 August 31, 2022 across Upper Indus catchment with maximum allowable lag of 2 days at the 95%
 457 CI. (The drivers are shown in the solid circles such as: DT= Dewpoint Temperature, ST= Surface
 458 Temperature, AT= Air Temperature, P= Precipitation intensity, SM= Snowmelt, RF= Runoff,
 459 NDWI= Normalized Difference Water Index, NDSI= Normalized Difference Snow Index, EVI=

460 Enhanced Vegetation Index: The node color represents autocorrelation whereas link color
461 represents the strength of directional link. The lag at which the link was found significant is shown
462 as link label, absence of which indicates that the link was found at zero lag).

463 4.5 Identifying moisture trajectories for the anomalous precipitation event

464 Based on moisture source uptake along trajectories for the observation period of July 1 to August
465 31, 2022, the amount of precipitation across the orographic ridges of the Upper Indus terrain was
466 delivered along two major pathways, one from Mediterranean Sea sources such as Western
467 disturbance (WD)-derived moisture during the onset of the monsoon and a second from the ISM,
468 originating from the Bay of Bengal and the Arabian Sea. The WD routes provided the moisture
469 sources for the precipitation along the 3000 m height trajectories, while the Arabian Sea, the Bay
470 of Bengal, and the Himalayan foreland provided the moisture along the 500 m and 1000 m
471 trajectories. Furthermore, the anomalous temperature gradient observed for the months of July and
472 August 2022 shows that the steep bedrock valleys are causing abnormal air-mass feedback. The
473 substantial divergence in the air-mass curve from mid-July to mid-August 2022 suggests there may
474 have been very high precipitation and temperature fluctuations during those periods (Fig. 11).



475

476 Fig.11. Moisture pathways (Backward trajectories) for Anomalous precipitation event from July 1
477 to August 31, 2022 across Upper Indus catchment: (Blue line denotes the trajectory of 500 m
478 elevation, yellow line denotes the trajectory of 1000 m elevation, and red line denotes the trajectory
479 of 3000 m elevation: Blue and yellow dot lines exhibit the ISM pathways, whereas Red dot lines
480 exhibit the WD pathways).

481 **5. Discussion**

482 **5.1 Spatial relationship between topographic metrics and event anomalies**

483 To characterize the geomorphic response of this extreme flood, we estimated stream power over
484 the trunk channel of the upper Indus River as an event anomaly. Understanding the spatial
485 distribution of stream power over the longitudinal profile of bedrock rivers is essential for
486 evaluating the catchment-scale variability in channel response to anomalous precipitation events
487 (Whipple et al., 2000; Kaushal et al., 2020). The peaks and troughs in the stream power profile
488 regulate the morphological characteristics of the bedrock channels (Schneider et al., 2014; Bawa
489 et al., 2014; Sinha et al., 2017). The river morphology and channel shape will be significantly
490 impacted by the temporal variations in flooding intensity during anomalous precipitation events
491 (Bookhagen and Strecker, 2012; Scherler et al., 2014).

492 The initial ~400–600 km length of the Upper Indus River is characterized by low gradient
493 channels as the river traverses over the elevated-low relief landscape. After traversing through the
494 mainstream and joining in the highest-order channel across the syntaxial region, there is a sharp
495 rise in the stream power profile along the downstream. The western syntax (NP-HM) in the NW
496 Himalayas is one of the most rapidly uplifting ($>\sim 5\text{-}10$ mm/y) and eroding ($>\sim 10$ mm/y) regions
497 on earth, with extreme topographic relief (>3000 m) (Fig. 1; 2). The sudden increase in the stream
498 power of the Upper Indus River after traversing through NP-HM and the resultant extreme flood
499 along lower middle reaches were also attributed to this high elevation change ($>\sim 4000$ m) and
500 steep channel gradient ($>\sim 20\text{-}30^\circ$) (Fig. 3b). The spatial variability of stream power is also highly
501 connected with other topographic metrics such as the k_{sn} and SL index, which demonstrate a
502 considerable rise in their longitudinal profiles when the channel crosses the NP-HM region (Fig.
503 3a). We observed that the stream power distribution along the longitudinal profiles of the Upper

504 Indus River is characterized by numerous peaks for both anomalous precipitation months in July
505 and August 2022 (Fig. 3b).

506 The upstream glaciated channels of the Trans Himalayan and Karakoram ranges have a
507 substantial glacial influence on erosion, contributing to the main trunk channel of the Upper Indus
508 River. Therefore, such high-magnitude floods ought to propagate through the channels of high
509 mountainous tributaries like Shyok, Gilgit, and Hunza, depending on the landscape characteristics
510 of the upper Indus catchment. A moderate change in the distribution pattern of snow cover may
511 have a significant impact on glacial runoff and substantially contribute to fluvial discharge. In
512 addition to the southern mountain front, the headwaters and syntaxial zone of the Upper Indus
513 catchment received a significant amount of precipitation, which contributed to the anomalous rise
514 in stream power and substantially contributed to this extreme flood that influenced the channel
515 geometry of the lower middle reach and drove high bedrock erosion (Fig. 4). However, the lower
516 middle reaches with higher stream power are distinguished by the steep channel valley and absence
517 of sediment deposition. The observation suggests that the higher-order channels of the Upper Indus
518 River traversing across higher relief and steep gradient valleys likely possess direct first-order
519 control over the pattern of erosion when combined with an anomalous rate of precipitation (Fig.
520 3b).

521 **5.2 Hydrological extremes and causal connections**

522 Our observations suggest that the interaction of glacial runoff with fluvial discharge over the steep
523 gradient channels combined to drive the extreme flood event across the Upper Indus catchment.
524 These extreme hydrological episodes imply that the possible response of atmospheric instabilities
525 may be elevation-dependent (Dimri et al., 2015; Forsythe et al., 2017; Ullah et al., 2021; Sharma
526 et al., 2021). It commenced with anomalous rises in temperature gradients over the glaciated sub-
527 catchments of the Upper Indus terrain, which drove the rapid changes in snow cover distribution
528 (Fig. 5; 6). This directly impacts glacial runoff magnitude and contributes to an anomalous rise in
529 fluvial stream power when traversed downstream over higher-relief fluvial reaches (Fig. 6). The
530 lower middle reaches of the Upper Indus catchment witnessed an anomalous amount of
531 precipitation intensity from early July to late August 2022 (Fig. 4). When compared to the annual
532 mean climatology, the precipitation intensity in the lower middle reaches of the Upper Indus River

533 was roughly ~150–200% higher in the 2022 monsoon period. The 2022 Upper Indus flood
534 represents an abrupt change from the region's prior precipitation and runoff patterns. To study this
535 anomaly, we utilized a Random Forest model trained on climatological data from the last 40 years
536 (1982-2021), with an emphasis on the months of July and August. The model used previous
537 climatology as a training dataset to estimate precipitation and runoff, which are significant drivers
538 of flooding. Despite the Random Forest model's resilience, the results revealed a substantial
539 difference between the model's predictions and the actual observed data obtained from the 2022
540 flood event. The model, based on 40 years of past data, failed to capture the high precipitation and
541 runoff patterns observed in July and August 2022 (Fig. 8: 9). The model's inability to predict
542 rainfall intensity, as well as subsequent runoff, highlights the anomalous nature of the event. This
543 disparity demonstrates that the 2022 flood was not only unusual but also went outside the typical
544 climatological shifts observed over the previous four decades. This emphasizes the necessity for
545 future modeling efforts to include other predictors, such as changes in snowmelt dynamics,
546 atmospheric circulation anomalies, and other non-stationary phenomena.

547 The moisture flux trajectories observed during the 2022 monsoonal period across the lower
548 middle reaches of the upper Indus River reveal two distinct sources of moisture pathways,
549 indicating that the combined effect of the westerlies-driven precipitation and the active monsoon
550 phase has likely caused this episodic event (Wang et al., 2017) (Fig. 11). Over the past years, the
551 interactions between moisture-laden ISM and southward-penetrating upper-level WD depression
552 have been linked to some catastrophic western Himalayan floods, such as in 2010 across Pakistan
553 and 2013 in Uttarakhand, India (Rasmussen and Houze, 2012; Vellore et al., 2015; Dimri et al.,
554 2016; Sharma et al., 2017). This anomalous rise in the rate of precipitation intensity contributes to
555 the rapid increase in stream power across steep valleys. The combined causal influence of
556 temperature and precipitation intensity with topography plays an important role in modulating such
557 episodic events, as these variables eventually regulate the amount of solid precipitation, influence
558 the change in snow cover, and have a significant impact on snowmelt runoff (Fig. 10) (Bovy et al.,
559 2016; Godard and Tucker, 2021; Delaney et al., 2023). This flood indicates the importance of
560 understanding the cause-and-effect relationship between temperature and precipitation in high-
561 elevation uplands.

562 **5.3 Channel Response to an Extreme Flood**

563 This study used the EVI change analysis as a significant event characteristic to capture the
564 changes in the channel morphology triggered by the 2022 Upper Indus flood. The anomalous
565 runoff events during the flood significantly altered channel geometry, and these changes were
566 reflected in the spatial and temporal variations of EVI (Fig. 6). Geomorphic processes such as
567 inundation, erosion, and landsliding have submerged or removed vegetation in areas marked by
568 drastic shifts in EVI ranges (Anderson and Goulden, 2011). The reduction in EVI ranges along the
569 steep channels highlights the expansion of water bodies during flooding, while the surrounding
570 areas experienced erosion and landslides due to the extreme discharge. The broader geomorphic
571 consequences of extreme hydrological events, such as river channel widening, sediment
572 deposition, and riverbank erosion, frequently link to these changes in vegetation cover (Olen et al.,
573 2016; Starke et al., 2020; Clift and Jonell, 2021; Scheip and Wegmann, 2021). While EVI cannot
574 directly measure hydrologic parameters, its ability to reflect the loss of vegetation makes it a useful
575 proxy for assessing the intensity of geomorphic processes during floods. This capability is
576 particularly important in high-mountain landscapes such as the Upper Indus, where steep
577 landscapes and glacial fluvial regimes amplify the effects of extreme events.

578 We utilize NDWI and EVI as change indicator metrics to understand the changes in channel
579 morphology due to this extreme flood event. The spatial variability of EVI corresponds
580 significantly with an increase in NDWI intensity downstream during July and August 2022 (Fig.
581 6). The substantial decrease in EVI values along downstream channels has also been attributed to
582 the anomalous precipitation event, which led to increased surface runoff, higher NDWI limits, and
583 subsequent flood deposits. We observed a significant direct causal influence with one-day-lagged
584 connection of precipitation and snowmelt on NDWI (Fig. 10). This combined causal relationship
585 between precipitation and snowmelt with NDWI intensity indicates that anomalous runoff
586 occurred across both glacial and fluvial channels. Further the inverse causal connection (negative
587 MCI ranges) between NDWI and EVI illustrates the rapid change in the channel geometry due to
588 increase in the fluvial discharge over lower middle reaches (Fig. 10).

589 The change in river morphology driven by the high-magnitude flood episodes is also
590 documented by the statistically significant ($p < 0.005$; $R = 0.81$) relationship observed between
591 anomalous stream power and relative EVI across the lower middle reaches of the Upper Indus
592 River (Fig. 7). It is generally assumed that relative vegetation intensity is an indicator of

593 geomorphic change that results from short-duration, high-magnitude hydrological events (Olen et
594 al., 2016; Starke et al., 2020; Clift and Jonell, 2021; Scheip and Wegmann, 2021). Thus, we
595 anticipate that EVI acts as a spatial indicator of change in the channel morphology across the lower
596 middle reaches of the trunk channel during the monsoon period of 2022 (Fig. 7) suggesting that
597 the distribution of event characteristics such as NDWI and EVI can be useful to detect the relative
598 change in channel morphology triggered by high-magnitude floods.

599 **6. Conclusion**

600 Our study reveals several significant event characteristics of the 2022 Upper Indus flood. Our
601 analysis shows that the Upper Indus flood originated across elevated glacial channels due to the
602 anomalous temperature rise, which increased the glacial runoff. This increase in runoff across
603 glaciated catchments after traversing through fluvial reaches enhanced the fluvial discharge and
604 likely increased the stream power in the anomalous precipitation region. The synoptic observation
605 of moisture pathways indicates that this anomalous precipitation incident is linked to the
606 interaction of southward moving mid-latitude westerlies troughs and eastward advancing
607 southwestern monsoon circulation. We observe a statistically significant relationship between the
608 anomalous stream power and relative EVI change across the lower middle reaches, which serves
609 as a significant geomorphic indicator of change in the channel morphology. This will aid in
610 determining the reliability of EVI as a consistent indicator of geomorphic changes, as well as its
611 applicability in studying the geomorphic evolution of regional landscapes. This extreme flood
612 illustrates how causal connections between temperature and precipitation across high relief-
613 gradient channels can magnify the impacts. Such hydrological events may play significant roles as
614 efficient geomorphic agents of erosion and, therefore, in the coupling of climatic extremes,
615 topography, and erosion. This study underscores the susceptibility of the elevated syntaxial region
616 to short-lived, high-magnitude flooding, indicating the need for additional research to determine
617 the causal relationship between the drivers of hydrological extremes. Significant research is needed
618 to understand the long-term impact of these extreme climatic events on the geomorphic processes
619 in the region.

620

621

622

623 **Code and data availability:**

624 The Data used and methodology section includes all of the open-source datasets and tools used in
625 the study.

626 **Author contribution:**

627 Abhishek Kashyap (AK): Conceptualization, Formal analysis, Methodology, writing – original
628 draft, Writing – review & editing.

629 Kristen L. Cook (KLC): Supervision, Visualization, Writing – review & editing

630 Mukunda Dev Behera (MDB): Supervision, Validation.

631 ***Competing interests**

632 The authors declare that they have no known competing financial interests or personal
633 relationships that could have appeared to influence the work reported in this paper. We wish to
634 confirm that there are no known conflicts of interest associated with this publication and there has
635 been no significant financial support for this work that could have influenced its outcome.

636 **Acknowledgments:** The authors acknowledge the authorities of IIT Kharagpur for facilitating the
637 study. AK thanks the Ministry of Education, Government of India, for the grant of a Ph.D.
638 Research Fellowship. AK thanks the IRD “South North Scheme” scholarship, managed by
639 Campus France, for the mobility and facilitation of a major part of this study at ISTERre, Université
640 Grenoble Alpes.

641

642

643

644

645

646

647 7. References

- 648 Adams, B.A., Whipple, K.X., Forte, A.M., Heimsath, A.M., Hodges, K.V., 2020. Climate
649 controls on erosion in tectonically active landscapes. *Sci. Adv.* 6, eaaz3166.
650 <https://doi.org/10.1126/sciadv.aaz3166>
- 651 Anderson, R.G., Goulden, M.L., 2011. Relationships between climate, vegetation, and
652 energy exchange across a montane gradient. *J. Geophys. Res.* 116, G01026.
653 <https://doi.org/10.1029/2010JG001476>
- 654 Archer, D., 2004. Hydrological implications of spatial and altitudinal variation in
655 temperature in the upper Indus basin. *Hydrology Research* 35, 209–222.
656 <https://doi.org/10.2166/nh.2004.0015>
- 657 Bai, L., Shi, C., Li, L., Yang, Y. and Wu, J., 2018. Accuracy of CHIRPS satellite-
658 rainfall products over mainland China. *Remote Sensing*, 10(3), p.362.
659 <https://doi.org/10.3390/rs10030362>
- 660 Bawa, N., Jain, V., Shekhar, S., Kumar, N., Jyani, V., 2014. Controls on morphological
661 variability and role of stream power distribution pattern, Yamuna River, western
662 India. *Geomorphology* 227, 60–72.
663 <https://doi.org/10.1016/j.geomorph.2014.05.016>
- 664 Benito, G., Macklin, M.G., Panin, A., Rossato, S., Fontana, A., Jones, A.F., Machado,
665 M.J., Matlakhova, E., Mozzi, P., Zielhofer, C., 2015. Recurring flood distribution
666 patterns related to short-term Holocene climatic variability. *Sci Rep* 5, 16398.
667 <https://doi.org/10.1038/srep16398>
- 668 Bhutto, F., 2022. The west is ignoring Pakistan’s super-floods. Heed this warning:
669 tomorrow it will be you. *The Guardian*.
- 670 Bookhagen, B., Burbank, D.W., 2006. Topography, relief, and TRMM-derived rainfall
671 variations along the Himalaya. *Geophysical Research Letters* 33, 2006GL026037.
672 <https://doi.org/10.1029/2006GL026037>
- 673 Bookhagen, B., Burbank, D.W., 2010. Toward a complete Himalayan hydrological
674 budget: Spatiotemporal distribution of snowmelt and rainfall and their impact on

675 river discharge. *J. Geophys. Res.* 115, 2009JF001426.
676 <https://doi.org/10.1029/2009JF001426>

677 Bookhagen, B., Strecker, M.R., 2012. Spatiotemporal trends in erosion rates across a
678 pronounced rainfall gradient: Examples from the southern Central Andes. *Earth*
679 *and Planetary Science Letters* 327–328, 97–110.
680 <https://doi.org/10.1016/j.epsl.2012.02.005>

681 Bookhagen, B., Thiede, R.C., Strecker, M.R., 2005a. Abnormal monsoon years and their
682 control on erosion and sediment flux in the high, arid northwest Himalaya. *Earth*
683 *and Planetary Science Letters* 231, 131–146.
684 <https://doi.org/10.1016/j.epsl.2004.11.014>

685 Bookhagen, B., Thiede, R.C., Strecker, M.R., 2005b. Late Quaternary intensified
686 monsoon phases control landscape evolution in the northwest Himalaya. *Geol* 33,
687 149. <https://doi.org/10.1130/G20982.1>

688 Bovy, B., Braun, J., Demoulin, A., 2016. A new numerical framework for simulating the
689 control of weather and climate on the evolution of soil-mantled hillslopes.
690 *Geomorphology* 263, 99–112. <https://doi.org/10.1016/j.geomorph.2016.03.016>

691 Breiman, L., 2001. [No title found]. *Machine Learning* 45, 5–32.
692 <https://doi.org/10.1023/A:1010933404324>

693 Burbank, D.W., Anderson, R.S., 2011. *Tectonic geomorphology*. John Wiley & Sons.

694 Butler, R.W.H., 2019. Tectonic evolution of the Himalayan syntaxes: the view from
695 Nanga Parbat. *SP* 483, 215–254. <https://doi.org/10.1144/SP483.5>

696 Clift, P.D., Jonell, T.N., 2021. Monsoon controls on sediment generation and transport:
697 Mass budget and provenance constraints from the Indus River catchment, delta
698 and submarine fan over tectonic and multimillennial timescales. *Earth-Science*
699 *Reviews* 220, 103682. <https://doi.org/10.1016/j.earscirev.2021.103682>

700 Cook, K.L., Andermann, C., Gimbert, F., Adhikari, B.R., Hovius, N., 2018. Glacial lake
701 outburst floods as drivers of fluvial erosion in the Himalaya. *Science* 362, 53–57.
702 <https://doi.org/10.1126/science.aat4981>

703 Delaney, I., Anderson, L., Herman, F., 2023. Modeling the spatially distributed nature of
704 subglacial sediment transport and erosion. *Earth Surf. Dynam.* 11, 663–680.
705 <https://doi.org/10.5194/esurf-11-663-2023>

706 Dimri, A.P., Chevuturi, A., Niyogi, D., Thayyen, R.J., Ray, K., Tripathi, S.N., Pandey,
707 A.K., Mohanty, U.C., 2017. Cloudbursts in Indian Himalayas: A review. *Earth-*
708 *Science Reviews* 168, 1–23. <https://doi.org/10.1016/j.earscirev.2017.03.006>

709 Dimri, A.P., Niyogi, D., Barros, A.P., Ridley, J., Mohanty, U.C., Yasunari, T., Sikka,
710 D.R., 2015. Western Disturbances: A review. *Reviews of Geophysics* 53, 225–
711 246. <https://doi.org/10.1002/2014RG000460>

712 Dimri, A.P., Yasunari, T., Kotlia, B.S., Mohanty, U.C., Sikka, D.R., 2016. Indian winter
713 monsoon: Present and past. *Earth-Science Reviews* 163, 297–322.
714 <https://doi.org/10.1016/j.earscirev.2016.10.008>

715 Fadil, A., 2022. Devastating floods in Pakistan claim lives of more than 500 children.
716 UNICEF.

717 Farinotti, D., Immerzeel, W.W., De Kok, R.J., Quincey, D.J., Dehecq, A., 2020.
718 Manifestations and mechanisms of the Karakoram glacier Anomaly. *Nat. Geosci.*
719 13, 8–16. <https://doi.org/10.1038/s41561-019-0513-5>

720 Forsythe, N., Fowler, H.J., Li, X.-F., Blenkinsop, S., Pritchard, D., 2017. Karakoram
721 temperature and glacial melt driven by regional atmospheric circulation
722 variability. *Nature Clim Change* 7, 664–670.
723 <https://doi.org/10.1038/nclimate3361>

724 Gao, F., Zhang, Y., Ren, X., Yao, Y., Hao, Z. and Cai, W., 2018. Evaluation of CHIRPS
725 and its application for drought monitoring over the Haihe River Basin, China. *Natural Hazards*,
726 92, pp.155-172. <https://doi.org/10.1007/s11069-018-3196-0>

727 Godard, V., Bourles, D.L., Spinabella, F., Burbank, D.W., Bookhagen, B., Fisher, G.B.,
728 Moulin, A., Leanni, L., 2014. Dominance of tectonics over climate in Himalayan
729 denudation. *Geology* 42, 243–246. <https://doi.org/10.1130/G35342.1>

730 Godard, V., Tucker, G.E., 2021. Influence of Climate-Forcing Frequency on Hillslope
731 Response. *Geophysical Research Letters* 48, e2021GL094305.
732 <https://doi.org/10.1029/2021GL094305>

733 Goodbred, S.L., Kuehl, S.A., Steckler, M.S., Sarker, M.H., 2003. Controls on facies
734 distribution and stratigraphic preservation in the Ganges–Brahmaputra delta
735 sequence. *Sedimentary Geology* 155, 301–316. [https://doi.org/10.1016/S0037-](https://doi.org/10.1016/S0037-0738(02)00184-7)
736 [0738\(02\)00184-7](https://doi.org/10.1016/S0037-0738(02)00184-7)

737 Hack, J.T., 1973. Stream-profile analysis and stream-gradient index. Journal of Research
738 of the us Geological Survey 1, 421–429.

739 Hewitt, K., 2007. Tributary glacier surges: an exceptional concentration at Panmah
740 Glacier, Karakoram Himalaya. J. Glaciol. 53, 181–188.
741 <https://doi.org/10.3189/172756507782202829>

742 Hewitt, K., 2009. Catastrophic rock slope failures and late Quaternary developments in
743 the Nanga Parbat–Haramosh Massif, Upper Indus basin, northern Pakistan.
744 Quaternary Science Reviews 28, 1055–1069.
745 <https://doi.org/10.1016/j.quascirev.2008.12.019>

746 Houze, R.A., Rasmussen, K.L., Medina, S., Brodzik, S.R., Romatschke, U., 2011.
747 Anomalous Atmospheric Events Leading to the Summer 2010 Floods in Pakistan.
748 Bulletin of the American Meteorological Society 92, 291–298.
749 <https://doi.org/10.1175/2010BAMS3173.1>

750 Immerzeel, W.W., Van Beek, L.P.H., Bierkens, M.F.P., 2010. Climate Change Will
751 Affect the Asian Water Towers. Science 328, 1382–1385.
752 <https://doi.org/10.1126/science.1183188>

753 Jaiswara, N.K., Kotluri, S.K., Pandey, A.K., Pandey, P., 2019. Transient basin as
754 indicator of tectonic expressions in bedrock landscape: Approach based on
755 MATLAB geomorphic tool (Transient-profiler). Geomorphology 346, 106853.
756 <https://doi.org/10.1016/j.geomorph.2019.106853>

757 Jaiswara, N.K., Kotluri, S.K., Pandey, P., Pandey, A.K., 2020. MATLAB functions for
758 extracting hypsometry, stream-length gradient index, steepness index, chi gradient
759 of channel and swath profiles from digital elevation model (DEM) and other
760 spatial data for landscape characterisation. Applied Computing and Geosciences
761 7, 100033. <https://doi.org/10.1016/j.acags.2020.100033>

762 Jones, B., 2022. How melting glaciers fueled Pakistan’s fatal floods.

763 Joshi, S.K., Kumar, S., Sinha, R., Rai, S.P., Khobragade, S., Rao, M.S., 2023. Identifying
764 moisture transport pathways for north-west India. Geological Journal 58, 4428–
765 4440. <https://doi.org/10.1002/gj.4759>

766 Kapnick, S.B., Delworth, T.L., Ashfaq, M., Malyshev, S., Milly, P.C.D., 2014. Snowfall
767 less sensitive to warming in Karakoram than in Himalayas due to a unique
768 seasonal cycle. *Nature Geosci* 7, 834–840. <https://doi.org/10.1038/ngeo2269>

769 Karmouche, S., Galytska, E., Runge, J., Meehl, G.A., Phillips, A.S., Weigel, K., Eyring,
770 V., 2023. Regime-oriented causal model evaluation of Atlantic–Pacific
771 teleconnections in CMIP6. *Earth Syst. Dynam.* 14, 309–344.
772 <https://doi.org/10.5194/esd-14-309-2023>

773 Kashyap, A., Behera, M.D., 2023. The influence of landslide morphology on erosion rate
774 variability across western Himalayan catchments: Role of westerlies and summer
775 monsoon interaction in the landscape characterization. *Geological Journal*
776 *gj.4913*. <https://doi.org/10.1002/gj.4913>

777 Kashyap, A., Behera, M.D., Pradhan, B., 2024. Differential surface uplift and knickpoint
778 evolution along the transient Teesta river in the eastern Himalayas. *Journal of*
779 *Asian Earth Sciences* 260, 105974. <https://doi.org/10.1016/j.jseaes.2023.105974>

780 Katsanos, D., Retalis, A. and Michaelides, S., 2016. Validation of a high-resolution
781 precipitation database (CHIRPS) over Cyprus for a 30-year period. *Atmospheric Research*, 169,
782 pp.459-464. <https://doi.org/10.1016/j.atmosres.2015.05.015>

783 Kaushal, R.K., Sarkar, A., Mishra, K., Sinha, R., Nepal, S., Jain, V., 2020. Spatio-
784 temporal variability in stream power distribution in the Upper Kosi River basin,
785 Central Himalaya: Controls and geomorphic implications. *Geomorphology* 350,
786 106888. <https://doi.org/10.1016/j.geomorph.2019.106888>

787 Khokhar, M.N., 2022. Rich countries caused Pakistan’s catastrophic flooding. Their
788 response? Inertia and apathy. *The Guardian*.

789 Kirby, E., Whipple, K.X., 2012. Expression of active tectonics in erosional landscapes.
790 *Journal of Structural Geology* 44, 54–75.
791 <https://doi.org/10.1016/j.jsg.2012.07.009>

792 Knox, J.C., 2000. Sensitivity of modern and Holocene floods to climate change.
793 *Quaternary Science Reviews* 19, 439–457. [https://doi.org/10.1016/S0277-](https://doi.org/10.1016/S0277-3791(99)00074-8)
794 [3791\(99\)00074-8](https://doi.org/10.1016/S0277-3791(99)00074-8)

795 Koons, P., Zeitler, P., Chamberlain, C., Craw, D., Meltzer, A., 2002. Mechanical links
796 between erosion and metamorphism in Nanga Parbat, Pakistan Himalaya.
797 *American Journal of Science* 302, 749–773.

798 Koons, P.O., Zeitler, P., Hallet, B., 2013. Tectonic aneurysms and mountain building.
799 *Treatise on geomorphology* 5, 318–349.

800 Korup, O., 2012. Earth’s portfolio of extreme sediment transport events. *Earth-Science*
801 *Reviews* 112, 115–125. <https://doi.org/10.1016/j.earscirev.2012.02.006>

802 Korup, O., Densmore, A.L., Schlunegger, F., 2010a. The role of landslides in mountain
803 range evolution. *Geomorphology* 120, 77–90.
804 <https://doi.org/10.1016/j.geomorph.2009.09.017>

805 Korup, O., Montgomery, D.R., 2008. Tibetan plateau river incision inhibited by glacial
806 stabilization of the Tsangpo gorge. *Nature* 455, 786–789.
807 <https://doi.org/10.1038/nature07322>

808 Korup, O., Montgomery, D.R., Hewitt, K., 2010b. Glacier and landslide feedbacks to
809 topographic relief in the Himalayan syntaxes. *Proc. Natl. Acad. Sci. U.S.A.* 107,
810 5317–5322. <https://doi.org/10.1073/pnas.0907531107>

811 Kretschmer, M., Runge, J., Coumou, D., 2017. Early prediction of extreme stratospheric
812 polar vortex states based on causal precursors. *Geophysical Research Letters* 44,
813 8592–8600. <https://doi.org/10.1002/2017GL074696>

814 Krich, C., Runge, J., Miralles, D.G., Migliavacca, M., Perez-Priego, O., El-Madany, T.,
815 Carrara, A., Mahecha, M.D., 2020. Estimating causal networks in biosphere–
816 atmosphere interaction with the PCMCI approach. *Biogeosciences* 17, 1033–
817 1061. <https://doi.org/10.5194/bg-17-1033-2020>

818 Lague, D., 2014. The stream power river incision model: evidence, theory and beyond.
819 *Earth Surf Processes Landf* 39, 38–61. <https://doi.org/10.1002/esp.3462>

820 Leland, J., Reid, M.R., Burbank, D.W., Finkel, R., Caffee, M., 1998. Incision and
821 differential bedrock uplift along the Indus River near Nanga Parbat, Pakistan
822 Himalaya, from ¹⁰Be and ²⁶Al exposure age dating of bedrock straths. *Earth and*
823 *Planetary Science Letters* 154, 93–107. [https://doi.org/10.1016/S0012-](https://doi.org/10.1016/S0012-821X(97)00171-4)
824 [821X\(97\)00171-4](https://doi.org/10.1016/S0012-821X(97)00171-4)

825 Leonard, J.S., Whipple, K.X., Heimsath, A.M., 2023a. Controls on topography and
826 erosion of the north-central Andes. *Geology*. <https://doi.org/10.1130/G51618.1>

827 Leonard, J.S., Whipple, K.X., Heimsath, A.M., 2023b. Isolating climatic, tectonic, and
828 lithologic controls on mountain landscape evolution. *Sci. Adv.* 9, eadd8915.
829 <https://doi.org/10.1126/sciadv.add8915>

830 Liu, P., Li, L., Guo, S., Xiong, L., Zhang, W., Zhang, J., Xu, C.-Y., 2015. Optimal design
831 of seasonal flood limited water levels and its application for the Three Gorges
832 Reservoir. *Journal of Hydrology* 527, 1045–1053.
833 <https://doi.org/10.1016/j.jhydrol.2015.05.055>

834 Ma, Y., Hu, X., Chen, Y., Hu, Z., Feng, T., Feng, G., 2023. Different Characteristics and
835 Drivers of the Extraordinary Pakistan Rainfall in July and August 2022. *Remote*
836 *Sensing* 15, 2311. <https://doi.org/10.3390/rs15092311>

837 Montgomery, D.R., Balco, G., Willett, S.D., 2001. Climate, tectonics, and the
838 morphology of the Andes. *Geol* 29, 579. [https://doi.org/10.1130/0091-](https://doi.org/10.1130/0091-7613(2001)029<0579:CTATMO>2.0.CO;2)
839 [7613\(2001\)029<0579:CTATMO>2.0.CO;2](https://doi.org/10.1130/0091-7613(2001)029<0579:CTATMO>2.0.CO;2)

840 Nanditha, J.S., Kushwaha, A.P., Singh, R., Malik, I., Solanki, H., Chuphal, D.S., Dangar,
841 S., Mahto, S.S., Vegad, U., Mishra, V., 2023. The Pakistan Flood of August 2022:
842 Causes and Implications. *Earth's Future* 11, e2022EF003230.
843 <https://doi.org/10.1029/2022EF003230>

844 Nawaz, M., Iqbal, M.F. and Mahmood, I., 2021. Validation of CHIRPS satellite-based
845 precipitation dataset over Pakistan. *Atmospheric Research*, 248, p.105289.
846 <https://doi.org/10.1016/j.atmosres.2020.105289>

847 NDMA, 2022. NDMA monsoon 2022 daily situation report No 093.

848 Nowack, P., Runge, J., Eyring, V., Haigh, J.D., 2020. Causal networks for climate model
849 evaluation and constrained projections. *Nat Commun* 11, 1415.
850 <https://doi.org/10.1038/s41467-020-15195-y>

851 Olen, S.M., Bookhagen, B., Strecker, M.R., 2016. Role of climate and vegetation density
852 in modulating denudation rates in the Himalaya. *Earth and Planetary Science*
853 *Letters* 445, 57–67. <https://doi.org/10.1016/j.epsl.2016.03.047>

854 Otto, F.E.L., Zachariah, M., Saeed, F., Siddiqi, A., Kamil, S., Mushtaq, H., Arulalan, T.,
855 AchutaRao, K., Chaithra, S.T., Barnes, C., Philip, S., Kew, S., Vautard, R.,

856 Koren, G., Pinto, I., Wolski, P., Vahlberg, M., Singh, R., Arrighi, J., Van Aalst,
857 M., Thalheimer, L., Raju, E., Li, S., Yang, W., Harrington, L.J., Clarke, B., 2023.
858 Climate change increased extreme monsoon rainfall, flooding highly vulnerable
859 communities in Pakistan. *Environ. Res.: Climate* 2, 025001.
860 <https://doi.org/10.1088/2752-5295/acbfd5>

861 Panda, S., Kumar, A., Das, S., Devrani, R., Rai, S., Prakash, K., Srivastava, P., 2020.
862 Chronology and sediment provenance of extreme floods of Siang River (Tsangpo-
863 Brahmaputra River valley), northeast Himalaya. *Earth Surf Processes Landf* 45,
864 2495–2511. <https://doi.org/10.1002/esp.4893>

865 Paredes-Trejo, F.J., Barbosa, H.A. and Kumar, T.L., 2017. Validating CHIRPS-based
866 satellite precipitation estimates in Northeast Brazil. *Journal of arid environments*, 139, pp.26-40.
867 <https://doi.org/10.1016/j.jaridenv.2016.12.009>

868 Piatrunia, N., 0000-0002-5341-7964, 2022. Glacial to Holocene climate variability in the
869 southern mid latitudes. <https://doi.org/10.26153/TSW/45137>

870 Rasmussen, K.L., Houze, R.A., 2012. A Flash-Flooding Storm at the Steep Edge of High
871 Terrain: Disaster in the Himalayas. *Bulletin of the American Meteorological*
872 *Society* 93, 1713–1724. <https://doi.org/10.1175/BAMS-D-11-00236.1>

873 Ray, K., Pandey, P., Pandey, C., Dimri, A., Kishore, K., 2019. On the recent floods in
874 India. *Current science* 117, 204–218.

875 Rossi, M.W., Whipple, K.X., Vivoni, E.R., 2016. Precipitation and evapotranspiration
876 controls on daily runoff variability in the contiguous United States and Puerto
877 Rico. *JGR Earth Surface* 121, 128–145. <https://doi.org/10.1002/2015JF003446>

878 Runge, J., 2018. Causal network reconstruction from time series: From theoretical
879 assumptions to practical estimation. *Chaos: An Interdisciplinary Journal of*
880 *Nonlinear Science* 28, 075310. <https://doi.org/10.1063/1.5025050>

881 Runge, J., Bathiany, S., Bollt, E., Camps-Valls, G., Coumou, D., Deyle, E., Glymour, C.,
882 Kretschmer, M., Mahecha, M.D., Muñoz-Marí, J., Van Nes, E.H., Peters, J.,
883 Quax, R., Reichstein, M., Scheffer, M., Schölkopf, B., Spirtes, P., Sugihara, G.,
884 Sun, J., Zhang, K., Zscheischler, J., 2019a. Inferring causation from time series in
885 Earth system sciences. *Nat Commun* 10, 2553. [https://doi.org/10.1038/s41467-](https://doi.org/10.1038/s41467-019-10105-3)
886 [019-10105-3](https://doi.org/10.1038/s41467-019-10105-3)

887 Runge, J., Gao, P., Garcin, F., Faltings, B., 2014. Churn prediction for high-value players
888 in casual social games, in: 2014 IEEE Conference on Computational Intelligence
889 and Games. Presented at the 2014 IEEE Conference on Computational
890 Intelligence and Games (CIG), IEEE, Dortmund, Germany, pp. 1–8.
891 <https://doi.org/10.1109/CIG.2014.6932875>

892 Runge, J., Gerhardus, A., Varando, G., Eyring, V., Camps-Valls, G., 2023. Causal
893 inference for time series. *Nat Rev Earth Environ* 4, 487–505.
894 <https://doi.org/10.1038/s43017-023-00431-y>

895 Runge, J., Nowack, P., Kretschmer, M., Flaxman, S., Sejdinovic, D., 2019b. Detecting
896 and quantifying causal associations in large nonlinear time series datasets. *Sci.*
897 *Adv.* 5, eaau4996. <https://doi.org/10.1126/sciadv.aau4996>

898 Scheip, C.M., Wegmann, K.W., 2021. HazMapper: a global open-source natural hazard
899 mapping application in Google Earth Engine. *Nat. Hazards Earth Syst. Sci.* 21,
900 1495–1511. <https://doi.org/10.5194/nhess-21-1495-2021>

901 Scherler, D., Bookhagen, B., Strecker, M.R., 2011. Spatially variable response of
902 Himalayan glaciers to climate change affected by debris cover. *Nature Geosci* 4,
903 156–159. <https://doi.org/10.1038/ngeo1068>

904 Schneider, J.M., Turowski, J.M., Rickenmann, D., Hegglin, R., Arrigo, S., Mao, L.,
905 Kirchner, J.W., 2014. Scaling relationships between bed load volumes, transport
906 distances, and stream power in steep mountain channels: Tracer Erlenbach. *J.*
907 *Geophys. Res. Earth Surf.* 119, 533–549. <https://doi.org/10.1002/2013JF002874>

908 Schwanghart, W., Scherler, D., 2014. Short Communication: TopoToolbox 2 –
909 MATLAB-based software for topographic analysis and modeling in Earth surface
910 sciences. *Earth Surf. Dynam.* 2, 1–7. <https://doi.org/10.5194/esurf-2-1-2014>

911 Shahid, M., Rahman, K.U., Haider, S., Gabriel, H.F., Khan, A.J., Pham, Q.B.,
912 Mohammadi, B., Linh, N.T.T. and Anh, D.T., 2021. Assessing the potential and hydrological
913 usefulness of the CHIRPS precipitation dataset over a complex topography in Pakistan.
914 *Hydrological Sciences Journal*, 66(11), pp.1664-1684.
915 <https://doi.org/10.1080/02626667.2021.1957476>

916 Shahzad, F., Mahmood, S.A., Gloaguen, R., 2009. Drainage network and lineament
917 analysis: An approach for Potwar Plateau (Northern Pakistan). *J. Mt. Sci.* 6, 14–
918 24. <https://doi.org/10.1007/s11629-009-0206-4>

919 Sharif, M., Archer, D.R., Fowler, H.J., Forsythe, N., 2013. Trends in timing and
920 magnitude of flow in the Upper Indus Basin. *Hydrol. Earth Syst. Sci.* 17, 1503–
921 1516. <https://doi.org/10.5194/hess-17-1503-2013>

922 Sharma, S., Sati, S.P., Basavaiah, N., Pandey, S., Sundriyal, Y.P., Rana, N., Singh, P.,
923 Pradhan, S., Shukla, A.D., Bhushan, R., Bhatt, R., Juyal, N., 2022. Mid to late
924 Holocene climate variability, forest fires and floods entwined with human
925 occupation in the upper Ganga catchment, India. *Quaternary Science Reviews*
926 293, 107725. <https://doi.org/10.1016/j.quascirev.2022.107725>

927 Sharma, S., Shukla, A.D., Bartarya, S.K., Marh, B.S., Juyal, N., 2017. The Holocene
928 floods and their affinity to climatic variability in the western Himalaya, India.
929 *Geomorphology* 290, 317–334. <https://doi.org/10.1016/j.geomorph.2017.04.030>

930 Sinha, R., Mohanta, H., Jain, V., Tandon, S.K., 2017. Geomorphic diversity as a river
931 management tool and its application to the Ganga River, India. *River Research &*
932 *Apps* 33, 1156–1176. <https://doi.org/10.1002/rra.3154>

933 Snyder, N.P., Whipple, K.X., Tucker, G.E., Merritts, D.J., 2003. Importance of a
934 stochastic distribution of floods and erosion thresholds in the bedrock river
935 incision problem. *J. Geophys. Res.* 108, 2001JB001655.
936 <https://doi.org/10.1029/2001JB001655>

937 Srivastava, P., Kumar, A., Chaudhary, S., Meena, N., Sundriyal, Y.P., Rawat, S., Rana,
938 N., Perumal, R.J., Bisht, P., Sharma, D., Agnihotri, R., Bagri, D.S., Juyal, N.,
939 Wasson, R.J., Ziegler, A.D., 2017. Paleofloods records in Himalaya.
940 *Geomorphology* 284, 17–30. <https://doi.org/10.1016/j.geomorph.2016.12.011>

941 Starke, J., Ehlers, T.A., Schaller, M., 2020. Latitudinal effect of vegetation on erosion
942 rates identified along western South America. *Science* 367, 1358–1361.
943 <https://doi.org/10.1126/science.aaz0840>

944 Tibau, X.-A., Reimers, C., Gerhardus, A., Denzler, J., Eyring, V., Runge, J., 2022. A
945 spatiotemporal stochastic climate model for benchmarking causal discovery

946 methods for teleconnections. *Environ. Data Science* 1, e12.
947 <https://doi.org/10.1017/eds.2022.11>

948 Ullah, W., Wang, G., Lou, D., Ullah, S., Bhatti, A.S., Ullah, S., Karim, A., Hagan,
949 D.F.T. and Ali, G., 2021. Large-scale atmospheric circulation patterns associated with extreme
950 monsoon precipitation in Pakistan during 1981–2018. *Atmospheric Research*, 253, p.105489.
951 <https://doi.org/10.1016/j.atmosres.2021.105489>

952 Vellore, R.K., Kaplan, M.L., Krishnan, R., Lewis, J.M., Sabade, S., Deshpande, N.,
953 Singh, B.B., Madhura, R.K., Rama Rao, M.V.S., 2016. Monsoon-extratropical
954 circulation interactions in Himalayan extreme rainfall. *Clim Dyn* 46, 3517–3546.
955 <https://doi.org/10.1007/s00382-015-2784-x>

956 Wang, N., Zeng, X.-M., Guo, W.-D., Chen, C., You, W., Zheng, Y., Zhu, J., 2018.
957 Quantitative diagnosis of moisture sources and transport pathways for summer
958 precipitation over the mid-lower Yangtze River Basin. *Journal of Hydrology* 559,
959 252–265. <https://doi.org/10.1016/j.jhydrol.2018.02.003>

960 Whipple, K.X., Hancock, G.S., Anderson, R.S., 2000. River incision into bedrock:
961 Mechanics and relative efficacy of plucking, abrasion, and cavitation. *Geological*
962 *Society of America Bulletin* 112, 490–503. [https://doi.org/10.1130/0016-
963 7606\(2000\)112<490:RIIBMA>2.0.CO;2](https://doi.org/10.1130/0016-7606(2000)112<490:RIIBMA>2.0.CO;2)

964 Whipple, K.X., Tucker, G.E., 1999. Dynamics of the stream-power river incision model:
965 Implications for height limits of mountain ranges, landscape response timescales,
966 and research needs. *J. Geophys. Res.* 104, 17661–17674.
967 <https://doi.org/10.1029/1999JB900120>

968 Wobus, C., Whipple, K.X., Kirby, E., Snyder, N., Johnson, J., Spyropoulou, K., Crosby,
969 B., Sheehan, D., 2006. Tectonics from topography: Procedures, promise, and
970 pitfalls, in: *Tectonics, Climate, and Landscape Evolution*. Geological Society of
971 America. [https://doi.org/10.1130/2006.2398\(04\)](https://doi.org/10.1130/2006.2398(04))

972 Wolfensberger, D., Gabella, M., Boscacci, M., Germann, U., Berne, A., 2021.
973 RainForest: a random forest algorithm for quantitative precipitation estimation
974 over Switzerland. *Atmos. Meas. Tech.* 14, 3169–3193.
975 <https://doi.org/10.5194/amt-14-3169-2021>

976 Wu, K., Liu, S., Jiang, Z., Liu, Q., Zhu, Y., Yi, Y., Xie, F., Ahmad Tahir, A., Saifullah,
977 M., 2021. Quantification of glacier mass budgets in the Karakoram region of
978 Upper Indus Basin during the early twenty-first century. *Journal of Hydrology*
979 603, 127095. <https://doi.org/10.1016/j.jhydrol.2021.127095>

980 Zeitler, P.K., Koons, P.O., Bishop, M.P., Chamberlain, C.P., Craw, D., Edwards, M.A.,
981 Hamidullah, S., Jan, M.Q., Khan, M.A., Khattak, M.U.K., Kidd, W.S.F., Mackie,
982 R.L., Meltzer, A.S., Park, S.K., Pecher, A., Poage, M.A., Sarker, G., Schneider,
983 D.A., Seeber, L., Shroder, J.F., 2001. Crustal reworking at Nanga Parbat,
984 Pakistan: Metamorphic consequences of thermal-mechanical coupling facilitated
985 by erosion. *Tectonics* 20, 712–728. <https://doi.org/10.1029/2000TC001243>

986 Zeitler, P.K., Meltzer, A.S., Brown, L., Kidd, W.S., Lim, C., Enkelmann, E., 2014.
987 Tectonics and topographic evolution of Namche Barwa and the easternmost Lhasa
988 block, Tibet, in: *Toward an Improved Understanding of Uplift Mechanisms and*
989 *the Elevation History of the Tibetan Plateau*. Geological Society of America
990 Special Papers, pp. 23–58.

991